BRNO UNIVERSITY OF TECHNOLOGY
VYSOKÉ UČENÍ TECHNICKÉ V BRNĚ

FACULTY OF MECHANICAL ENGINEERING
FAKULTA STROJNÍHO INŽENÝRSTVÍ

INSTITUTE OF PHYSICAL ENGINEERING
ÚSTAV FYZIKÁLNÍHO INŽENÝRSTVÍ

OPTICAL CHARACTERIZATION OF INORGANIC LEAD HALIDE PEROVSKITES USING AB-INITIO METHODS
OPTICKÁ CHARAKTERIZACE ANORGANICKÝCH OLOVNATÝCH HALOGENIDOVÝCH PEROVSKITŮ POMOCÍ AB-INITIO METOD

BACHELOR'S THESIS
BAKALÁŘSKÁ PRÁCE

AUTHOR
AUTOR PRÁCE

Radovan Matula

SUPERVISOR
VEDOUCÍ PRÁCE

Ing. Petr Liška

BRNO 2022

Assignment Bachelor's Thesis

Institut:	Institute of Physical Engineering
Student:	**Radovan Matula**
Degree programm:	Physical Engineering and Nanotechnology
Branch:	no specialisation
Supervisor:	**Ing. Petr Liška**
Academic year:	2021/22

As provided for by the Act No. 111/98 Coll. on higher education institutions and the BUT Study and Examination Regulations, the director of the Institute hereby assigns the following topic of Bachelor's Thesis:

Optical characterization of inorganic lead halide perovskites using ab–initio methods

Brief Description:

Lead halide perovskites (LHPs) are advanced materials that have received much attention in the last decade due to their application potential, especially in photovoltaics and optoelectronics. LHPs are semiconducting materials with a direct bandgap with unique optical and structural properties. Although LHPs are some of the most cited materials of the last decade, the origin of all their unique properties is still not completely physically elucidated. This bachelor thesis should deal with the application of ab–initio calculations in an effort to clarify some structural properties of LHPs such as their band structure, the density of states, or optically active phonon modes. The theoretically obtained results should then be compared with experimental values.

Bachelor's Thesis goals:

1) Carry out a research study on the topic of inorganic lead halide perovskites (CsPbX3, X = Cl, Br, I).
2) Carry out a research study on the topic of ab–initio calculations in the VASP program, which allow optical characterization of crystal structures.
3) Using ab–initio methods, optically characterize inorganic lead halide perovskites (band structure, density of states, dispersion relations of phonons, effective mass of excitons).
4) Compare the obtained results with the available experimental data.

Recommended bibliography:

BECKER, M., VAXENBURG, R., NEDELCU, G. et al. 2018. Bright triplet excitons in caesium lead halide perovskites. Nature 553, 189–193.

DEY, Amrita, Junzhi YE, Apurba DE, et al. 2021. State of the Art and Prospects for Halide Perovskite Nanocrystals. ACS Nano. 15(7), 10775-10981.

IBACH, H. a Hans LÜTH. Solid-state physics: an introduction to principles of materials science. 4th ed. Berlin: Springer-Verlag, c2009. ISBN 978-3-540-93803-3.

Deadline for submission Bachelor's Thesis is given by the Schedule of the Academic year 2021/22

In Brno,

L. S.

_____	_____
prof. RNDr. Tomáš Šikola, CSc.	doc. Ing. Jaroslav Katolický, Ph.D.
Director of the Institute	FME dean

Abstract

This thesis deals with lead halide perovskites (LHPs), a relatively new group of materials which have found much use in fields such as photovoltaics and optoelectronics. LHPs' potential lies in their electronic structure and easily tunable band gap, which result in unique physical and functional properties. To study LHPs' optical properties and electronic structure we employ density functional theory (DFT). The DFT method is an ab-initio method built upon minimization of electron density functional to find the ground state energy of a given system. The DFT method was employed along with the use of hybrid functionals to obtain the correct band structure and band gap of $CsPbBr_3$ bulk. The theoretically obtained data were used in the effective mass model to compare with the photoluminescence emission peaks of individual $CsPbBr_3$ nanocrystals to correctly assess the exciton energy levels based on the nanocrystals' size, and shape.

Abstrakt

Tato práce se zabývá olovnato-halogenidovými perovskity (OHP), novou skupinou materiálů, jež našla své využití v oblastech jako například fotovoltaika a optoelektronika. Potenciál OHP leží v jejich elektronové struktuře a snadno laditelném zakázaném pásu, což má za následek jedinečné fyzikální a funkční vlastnosti. Ke studiu optických vlastností a elektronové struktury OHP využíváme teorie funkcionálu hustoty (DFT). DFT metoda je ab-initio metoda založená na principu minimalizace funkcionálu elektronové hustoty k nalezení základní energie daného systému. DFT metoda společně s hybridními funkcionály byla využita pro získání správné elektronové struktury a hodnoty zakázaného pásu pro krystal $CsPbBr_3$. Teoreticky získaná data byla využita v modelu efektivní hmotnosti k porovnání s fotoluminiscenčními spektry jednotlivých $CsPbBr_3$ nanokrystalů s cílem zjistit energiové hladiny excitonů v závislosti na velikosti a tvaru nanokrystalů.

Keywords

lead halide perovskites, $CsPbBr_3$, density functional theory

Klíčová slova

olovnato-halogenidové perovskity, $CsPbBr_3$, teorie funkcionálu hustoty

I hereby declare I have written this bachelor thesis under the guidance of my thesis supervisor and that I have not used any sources other than those listed in the bibliography and identified as references.

Radovan Matula

Acknowledgement

<div align="right">Radovan Matula</div>

Contents

Introduction

The year was 1839 when Gustav Rose and his team of scientists in the Ural Mountains discovered a mineral $CaTiO_3$ that would come to be known as *Perovskite*. It wasn't until 1945 when the now well-known perovskite structure was first described using X-ray diffraction giving the first impulse for the creation of a whole category of materials, called perovskites, sharing the same structure ABX_3. Then, for over 60 years, all was quiet on the perovskite front until a team of Japanese scientists chose a lead halide perovskite (LHP) to be the basis of their solar cell. Their results didn't captivate the attention of the wider scientific community at first, but the promise this material held piqued enough interest to guarantee further study. Since its publishing, the number of citations of the very first paper by Kojima and Miyasaka et al. rose exponentially. It is them to whom we owe the beginning of the 'age of perovskite'.

With LHPs' rise to prominence came the discovery of the unique and sometimes unheard-of qualities this group of materials has to offer. In the subsequent years, these unique qualities ensured LHPs found their application in a whole host of fields, the most significant being the very field they first started in, photovoltaics. As the demand for better, more stable and more efficient LHPs boomed, LHPs saw great improvement both in their chemical composition and means of production. All this led to the group of perovskites we study in this thesis, LHPs $CsPbX_3$ (X = Cl, Br, I).

At this time and age, LHPs and perovskites as a whole are quite well understood from an experimental standpoint, as the material's fascinating qualities warranted thorough experimental studies from scientists all over the world. However, there is still more to be understood and that can be done through the employment of various ab-initio [1] methods which can uncover the reasons behind experimentally observed phenomena. One way to study material theoretically is through the employment of density functional theory (DFT) calculations. By using the DFT method to study LHPs' theoretical band structure and optical properties one can at least partially examine the physics behind the material's distinctive properties, by comparing the calculated data to experimentally obtained results of photoluminescence spectroscopy.

This thesis seeks to provide a comprehensive study of lead halide perovskites, a type of material with a direct band gap and unique properties, and shed some light on the reasons behind those properties. To do so we shall apply an array of ab-initio calculations, which we are then comparing to experimental data.

---

[1] from Latin, means *from the beginning* and in the scientific context used as *from first principles*

1. Electron Structure of Solid Matter

In this chapter, we look at the electronic structure of solids. This theory forms the cornerstone for density functional theory (DFT) and other ab-initio calculations, which are the main tools used in this thesis.

1.1 Schrödinger equation

The Schrödinger equation (SE) provides a full description of eigenstates and eigenfunctions of a given isolated quantum system via its solution, the wave function $\Psi = \Psi(r_1, r_2, \cdots, r_m; t)$, where m is the number of particles. The general form is the time-dependent SE

$$i\hbar\frac{\partial\left|\Psi\right\rangle}{\partial t} = \hat{\mathbf{H}}\left|\Psi\right\rangle, \tag{1.1}$$

where $\hbar$ is the reduced Planck constant and $\hat{\mathbf{H}}$ is Hamilton's operator, also known as *Hamiltonian*. For stationary problems, we can express the time-independent SE as

$$\hat{\mathbf{H}}\left|\Psi\right\rangle = E\left|\Psi\right\rangle, \tag{1.2}$$

where E is the eigenvalue of a given Hamiltonian $\hat{\mathbf{H}}$.

The Hamiltonian is the operator of the total energy of a system. It consists of operators for kinetic and potential energy.

1.1.1 Born-Oppenheimer approximation

Equation 1.1 describes the given system perfectly from the physical standpoint. However, in doing so, it renders the problem virtually unsolvable. One big complication is the fact that the movements of nuclei and electrons are bound together by a single wave function. That is where the Born-Oppenheimer approximation comes into play.

The Born-Oppenheimer approximation is built on the notion of the mass of the nuclei being much greater compared to the mass of the electrons, which means the nuclei move at a much slower rate than the electrons. The approximation goes as far as considering the nuclei static in relation to the electrons. This allows for the wave function to be split into nuclear and electronic components as follows

$$|\Psi(\mathbf{r}_1, \cdots, \mathbf{r}_n; \mathbf{R}_1, \cdots, \mathbf{R}_m)\rangle = |\Psi_{\mathrm{e}}(\mathbf{r}_1, \cdots, \mathbf{r}_n; \{\mathbf{R}_1, \cdots, \mathbf{R}_m\})\rangle \cdot |\Psi_{\mathrm{n}}(\mathbf{R}_1, \cdots, \mathbf{R}_m)\rangle. \tag{1.3}$$

Vectors $\mathbf{r}_i$ $(i = 1, 2, \cdots, n)$ and $\mathbf{R}_l$ $(l = 1, 2, \cdots, m)$ define positions of electrons and nuclei, respectively and Ψ_{e}, Ψ_{n} denote the wave functions for electrons and nuclei. $\{R_l\}$ in Ψ_e serves only as a parameter, implying that the distribution of electrons is dependent solely on the position of nuclei and not on their velocity [1]. However even after the Born-Oppenheimer approximation the SE is unsolvable in most cases but for a few simple ones. That is why further approximation is needed, such as DFT or Hartree-Fock presented later in this thesis.

Equation 1.4 shows the Hamiltonian of a system relevant to DFTs, i.e., isolated N-electron system of atoms or molecules, it is important to note the following equations are in Hartree's atomic units,

$$\hat{\mathbf{H}} = \hat{\mathbf{T}} + \hat{\mathbf{V}} + \hat{\mathbf{V}}_{\mathrm{c}} = \sum_{i=1}^{N} \left(-\frac{1}{2}\nabla_i^2 \right) + \sum_{i=1}^{N} v(r_i) + \sum_{i<j}^{N} \frac{1}{r_{ij}} \tag{1.4}$$

in which

$$\hat{\mathbf{T}} = \sum_{i=1}^{N} \left(-\frac{1}{2}\nabla_i^2 \right) \tag{1.5}$$

is the kinetic energy operator,

$$\hat{\mathbf{V}}_{\mathrm{c}} = \sum_{i<j}^{N} \frac{1}{r_{ij}}, \tag{1.6}$$

is the potential generated by the Coulomb interaction and $\hat{\mathbf{V}}$ is the external potential generated by the surrounding positively charged nuclei, where

$$v(r_i) = -\sum_{\alpha} \frac{Z_\alpha}{r_{i\alpha}} \tag{1.7}$$

is the potential caused by charges Z_α of the surrounding nuclei which acts on the i-th electron and $r_{i\alpha}$ is the distance between the i-th electron and the nuclei with charge Z_α [2, 3].

1.2 Bloch's theorem

The basis of a crystal structure is formed by an atom or a group of atoms. The basis repeats ad infinitum, forming the entire lattice and consequently resulting in periodic potential which acts upon the charge carriers. Bloch's theorem states that the wave function of any periodic system can be expressed as

$$\Psi(\mathbf{r}) = u(\mathbf{r}) \cdot e^{\mathbf{ik}\cdot\mathbf{r}}, \tag{1.8}$$

where $\mathbf{k}$ is the wave vector and $u(\mathbf{r})$ serves as a periodic function with the period of the lattice $u(\mathbf{r}) = u(\mathbf{r} + \mathbf{T})$, $\mathbf{T}$ is the translation vector of the lattice, which defines the atoms' positions in relation to each other, thus defining the whole crystal lattice [4].

Due to Bloch's theorem the $e^{i\mathbf{k}\cdot\mathbf{r}}$ term enters the SE and brings with it dependence on $\mathbf{k}$, which consequently means $E \sim |\mathbf{k}|$. Direct result of this is formation of electronic band structure.

1.3 Electronic band structure

In quantum mechanics, electrons can inhabit only certain discrete levels in an atom's electron shell. When we put a great number of atoms together to form a crystal lattice, the ever-so-slightly misaligned electron levels will create a continuum of energy - bands - in which electrons are allowed to exist. The regions between the bands containing no energy levels are called *forbidden*. The width of a band gap defines the material's type, this categorization is shown in Figure 1.1.
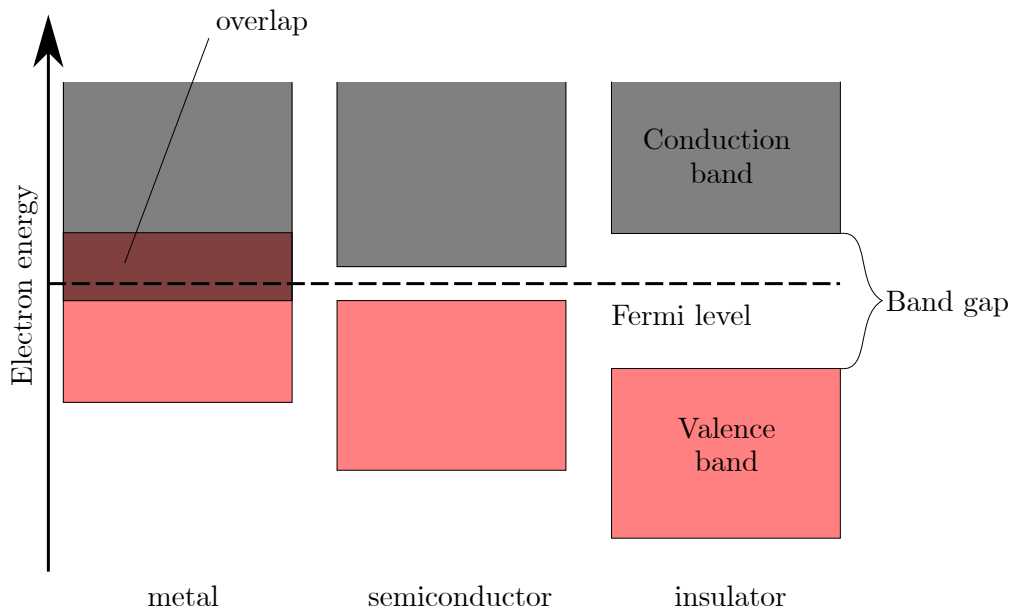
Figure 1.1: Schematic image of the relation of the valence and the conduction bands to each other in different types of materials. In metals the band edges border on each other or even the bands overlap, thus making the conduction possible without any added energy. Semiconductors have a band of forbidden energies, the band gap, therefore requiring excitation energy to allow the electrons to be excited into the conduction band. Insulators exhibit the band gap so wide the electrons cannot cross it to facilitate conduction. Adapted and edited from [5].

The energy gap called the *band gap* is defined as the difference between the maximum of the valence band and the minimum of the conduction band. The band gap is of great interest as it determines the energy an electron needs to transition between the valence and conduction bands.

The valence band, located under the Fermi level, is the highest occupied band at absolute zero, whereas the conduction band, above the Fermi level, is unoccupied. As the temperature increases, more electrons are thermally excited and cross the band gap into the conduction band where they can move freely through the material. The Fermi level E_F is the highest occupied state at $0\,K$ and its proximity to the conduction band determines the probability of transition for the valence band electrons.

Metals exhibit band gap of $E_g \approx 0$. Insulators are materials with band gap over 3 eV. Semiconductors (SCs) find themselves approximately in between these two, with the width of their band gap being (0–4) eV [4, 6]. SC's optical properties are influenced by the width of the band gap. There are two main types of band gaps in SCs, which are discussed in the following section.

1.3.1 Direct & indirect band gap

The energy states at the valence band maximum and conduction band minimum are defined by their k-vectors and their value determines the transition, as shown in Figure 1.2. For *direct* band gap the values of electron and hole k-vectors are equal, the electron can undergo an optical transition. Whereas in *indirect* band gap the values of k-vectors are not equal, part of the momentum must be dissipated via phonons first. Only then can the electron make the transition, however, the light emission is very low. All the optical transitions are governed by the energy and momentum conservation laws [2, 7].

1.4 Density of states

The density of states (DOS) is given by the number of states per unit volume per unit energy. The mentioned volume is the volume enclosed by a constant energy surface in $\mathbf{k}$-space. For free electrons in an isotropic environment, E and $\mathbf{k}$ are connected by the dispersion relation

$$E(\mathbf{k}) = \frac{\hbar^2 \mathbf{k}^2}{2m}. \tag{1.9}$$

This relation serves as the bridge between the two systems used to describe DOS. The number of states is equal in both systems.

The $\mathbf{k}$-space (reciprocal) is the Fourier transform of the real space. These two spaces are inversely related as given by $k = 2\pi/\lambda$, $k = |\mathbf{k}|$. The reciprocal lattice is formed by periodic repetition of the first Brillouin zone. A Brillouin zone is the reciprocal counterpart to Wigner-Seitz cell and it is a primitive cell defined by points of high symmetry. As a result of Bloch's theorem, any system is completely characterised by its behaviour in the Brillouin zone.
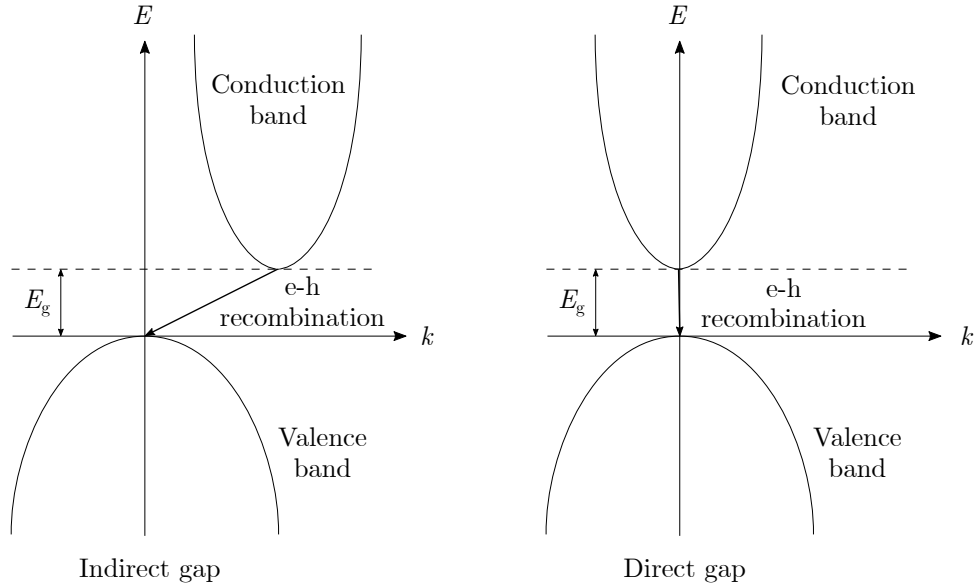
Figure 1.2: Schematic of the direct and indirect band gaps. In the case of the indirect band gap the k-vectors at the valence band maximum and the conduction band minimum are not equal, part of the momentum must be dissipated first via phonons before the transition is allowed. For the direct band gap, the k-vectors have the same value, the electron can transition to the higher band when it absorbs a photon with enough energy. Adapted and edited from [7].

The states in an energy band are not distributed evenly, therefore there will be areas with a higher concentration of energy states as illustrated in Figure 1.3. The DOS of a given system yields the approximate number of available quantum states. The Fermi-Dirac distribution gives us the probability of a given quantum state being occupied. Combining these two allows us to determine the density of occupied states.
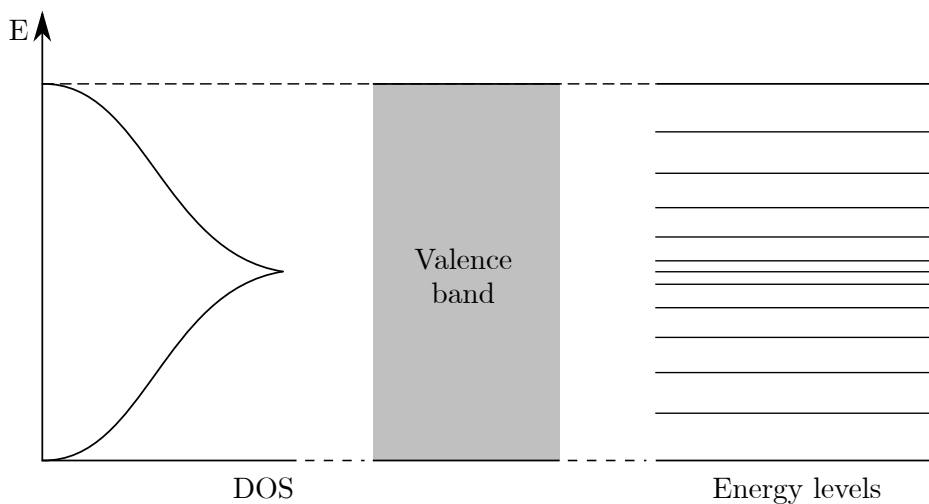
Figure 1.3: Schematic of the DOS of an arbitrary valence band. The left part pictures the DOS in relation to energy. On the right are the idealised energy levels (depicted as lines) distributed throughout the width of the band with varying density, the densest area is in the centre of the band coinciding with the graph on the left. Adapted and edited from [7].

The knowledge of quantum state occupancy is important for understanding the optical properties of a material. The DOS resulting from a DFT calculation provides us with the understanding of which electron orbitals participate in the formation of valence and conduction bands [3, 4, 7].

1.5   Effective mass

An electron moving through the periodic potential of a crystal lattice will have a different perceived mass than an electron in a vacuum. This 'different' mass is called *effective* mass and it is given by the following expression

$$\frac{1}{m^*} = \frac{1}{\hbar^2}\frac{\mathrm{d}^2 E}{\mathrm{d}\mathbf{k}^2},\tag{1.10}$$

where $\frac{\mathrm{d}^2 E}{\mathrm{d}\mathbf{k}^2}$ expresses the change in the slope of the E-$\mathbf{k}$ curve given by the dispersion relation, meaning the effective mass changes with the electron's position within the band. Using the effective mass in the classical mass's stead allows for the electron's movement through the lattice to be described by Newton's second law [7].

A particle's effective mass can be either positive or negative, the sign, however, has nothing to do with the particle's actual mass, rather it serves as correction in the case of a hole. For both the electron and the hole, the effective mass usually measures between 0.1–10 expressed in units of m_{e}, the electron rest mass.

We use the effective mass model to approximate the band edges of conduction and valence bands. In our case the approximation is parabolic

$$E(\mathbf{k}) = E_{\mathrm{g}} \pm \frac{\hbar^2\mathbf{k}^2}{2m^*},\tag{1.11}$$

where E_{g} is the energy of the band gap, plus and minus denote an electron or a hole, respectively [4, 7].

1.6   Excitons

An electron-hole pair bound together by the Coulomb attractive interaction is called an *exciton*. In direct processes the threshold for exciton formation is $\hbar\omega > E_{\mathrm{g}}$, whereas in the indirect ones we have to take into account phonon interaction, therefore lowering the needed energy by $\hbar\Omega$; $\hbar\omega$ is the energy absorbed by the electron, while $\hbar\Omega$ is the energy of phonons.

Exciton is an electrically neutral quasiparticle, meaning it does not transfer any net charge. However, an exciton carries the energy of its bond, which it releases in the form of a photon once the exciton inevitably decays by recombination [4, 1].

Depending on the type of material, we distinguish between two types of excitons. The Frenkel exciton is found in insulators and is also known as a tightly bound exciton, due to the pair's excitation being localized (usually to a single atom). The Mott-Wannier excitons, typical for semiconductors, are considered weakly bound as

the exciton radius is much greater than the lattice parameter [8, 9, 10].

The exciton radius, i.e., the distance between the electron and the hole, depends on the effective masses of both particles, thus dependent on the shape of the band structure [11].

1.7 Photoluminescence

Photoluminescence (PL) is a type of luminescence, i.e, spontaneous emission of light from any form of matter, caused by the absorption of photons [11]. The process of PL consists of three steps. Photoexcitation is the event of a photon supplying an electron with enough energy to allow it to be excited to a higher level. During relaxation, part of the system's energy is dissipated via phonon scattering, which leads to the creation of electron and hole populations in the conduction and the valence band, respectively. Finally, radiative recombination, i.e., the recombination of holes and electrons accompanied by the emission of photons. The process is shown in Figure 1.4.
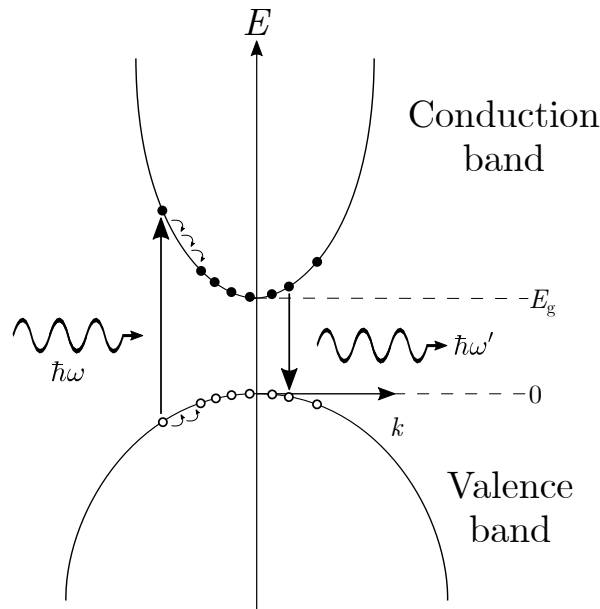
Figure 1.4: Schematic depicting the process of PL. The electron absorbs a photon of sufficient energy $\hbar\omega$ to overcome the band gap and transitions into the higher band. Here is where the relaxation occurs and part of the system's energy is dissipated via phonon scattering. Finally, the electron recombines with the hole which is accompanied by the emission of a photon with energy $\hbar\omega'$. Adapted and edited from [11].

PL can be classified into two main categories in respect to the nature of the electronic transitions causing it: intrinsic and extrinsic. Intrinsic PL can be further divided into three subcategories. Band-to-band PL is the result of the recombination of an electron in the conduction band and a hole in the valence band. Exciton PL is caused by the recombination of an exciton. Due to the nature of excitons, the exciton PL can be observed only at temperatures low enough for the excitons to be stable.

Cross-luminescence is produced when the recombination of an electron in the valence band and a hole in the outermost core band occurs. This type of PL happens only

in a select few materials, for example, BaF_2, which satisfy the condition $E_{\text{c-v}} < E_{\text{g}}$, i.e, the difference between the outermost core band and the top of the valence band is lesser than the band gap.

Extrinsic PL is caused by the presence of impurities or defects in the lattice and there are two forms which can be observed. In the case of localised PL, the luminescence processes are confined to a specific luminescence centre, which is usually synonymous with the disorder. Unlocalised PL means the free electrons and holes in the conduction band and the valence band, respectively, partake in the process.

Another way to sort PL is by the difference between the energy of an absorbed and emitted photon, described by the Stokes shift. Stokes shift means the emission of a photon of lower energy, i.e., longer wavelength. Contrastingly, the anti-Stokes shift is the situation of the emitted photon having higher energy compared to the absorbed one. The energy difference is accounted for by the dissipation of thermal phonons in the lattice [8, 12].

2. Lead Halide Perovskites

Perovskites as a group of materials are named after calcium titanate, also known as Perovskite, owing to the lattice structure, which they share with the mineral. The perovskite structure's composition is given as ABX_3. Seeing as in this work, we focus on a subgroup of perovskites called lead halide perovskites (LHP), the formula becomes $CsPbX_3$, where X stands for Cl, Br, or I.

2.1 Structural properties

The LHPs we study crystallise at room temperature in an orthorhombic lattice. The structure is built from PbX_6 octahedra forming a cubic lattice with cations Cs^+ filling the cavities that are created when the octahedra are stacked together, as is shown in Figure 2.1.
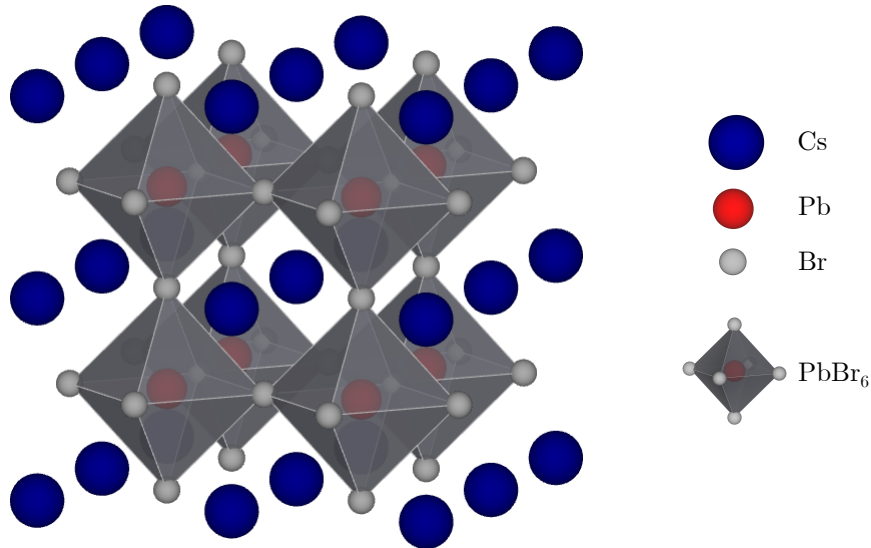
Figure 2.1: Schematic of the cubic structure of a $CsPbX_3$ perovskite, formed by the PbX_6 octahedra and completed by the Cs cations' presence in the cavities among the octahedra. The lattice parameter of the $CsPbBr_3$ crystal is $a = 5.92$ Å and the volume of the primitive cell is $V = 207.475$ Å^3. The distance between the Br and Cs atoms is $d_{Br\text{-}Cs} = 4.23$ Å and the distance between the Br and Pb atoms is $d_{Br\text{-}Pb} = 3.02$ Å Created with VESTA [13].

The general guideline when it comes to regular SCs is to keep the occurrence of impurities and crystalline defects as low as possible. LHPs however can contain up

to 1–2 atomic per cent of point defects, such as vacancies, and still keep their unique properties. This shows LHPs are highly tolerant to defects [14].

The high tolerance is the result of a combination of several factors. The main one is, that the vacancies at A- or X-sites require very low formation energy and are therefore the dominant type of defect in the perovskite lattice. These vacancies unlike in conventional SCs do not form mid-gap trap states, as is shown in Figure 2.3, thus not influencing the material's optical and electronic properties. Furthermore, the vacancies serve as a major enabling factor for the LHPs' bright PL [8, 14, 15].

LHP's phase depends on temperature as shown in Figure 2.2 [16]. If we look at $CsPbBr_3$, as it is the LHP we examine closely in this work, we see it is orthorhombic at the room temperature, however when conducting the DFT calculations we consider cubic lattice for simplicity.
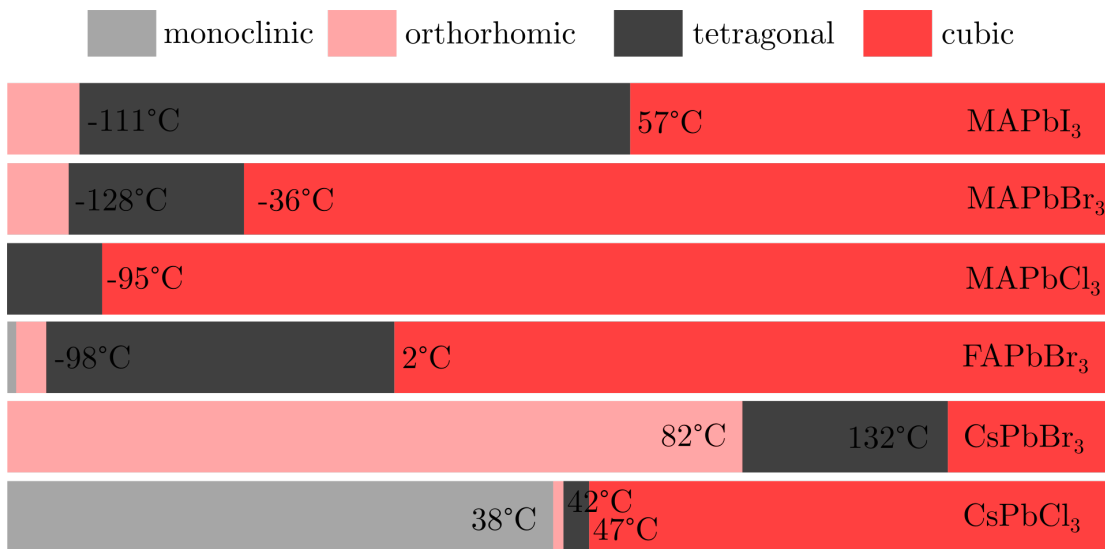
Figure 2.2: Schematic of the thermal dependency of phase transitions in different LHPs. Adapted and edited from [16].

2.2 Electronic properties

The LHPs are a family of SCs with direct and highly tunable band gap. The electrons in LHPs do not behave as a classical electron gas, for they are believed to be strongly correlated, instead, they are governed by electron-electron interactions. Changes in the electron behaviour as significant as these result in interesting phenomena such as unprecedented PL quantum yields in LHPs, metal-insulator transitions or high-temperature superconductivity in more advanced compounds [17, 18, 19]. The band gap in $CsPbBr_3$ crystal, as the structure we study, is $E_g = 2.36$ eV.

The composition of bands is shown in Figure 2.3. The top of the valence band is formed as a combination of Pb 6s and Br 4p orbitals with overall s-symmetry and the bottom of the conduction band is formed by Pb 6p orbitals resulting in an overall p-symmetry.
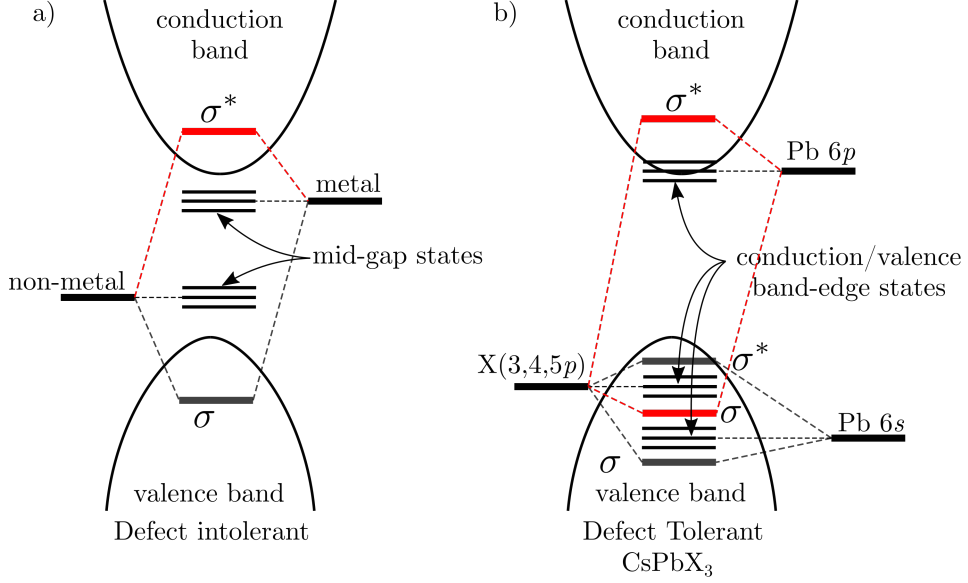
Figure 2.3: Schematic of the energy bands in materials a) intolerant to defects b) tolerant to defects – LHPs. LHPs unlike regular SCs do not exhibit mid-band gap states which would influence the material's optical properties. In LHPs the top of the valence band is formed by Pb 6s orbitals, resulting in overall s-symmetry, and the bottom of the conduction band is formed by Pb 6p orbitals resulting in p-symmetry and facilitating the spin-orbital coupling. Adapted and edited from [8].

The lead in the structure is the reason behind strong spin-orbital coupling. The first and the most significant effect spin-orbital coupling has on the calculation is a massive reduction of the band gap. The other effect we registered, which is closely related to the band gap reduction, was the splitting of the conduction band minimum level into two, one forming the bottom of the conduction band and a split-off band [20].

2.3   Optical properties

Nanostructured SCs emit light by means of excitons. The ground state exciton in a conventional SC is, according to Hund's rules, poorly emitting. This, however, is not what experiments have shown in LHPs. The lowest energy exciton in LHPs is a bright triplet [21].

One of the main reasons behind this unusual behaviour is the effect of strong spin-orbital coupling. Lead as a heavy metal helps in the formation of the unique band structure that ensures LHPs' great qualities. Taking spin into account, a hole can occupy two states: up and down

$$J_{\mathrm{h}} = \frac{1}{2} : |\uparrow\rangle_h = |S\rangle |\uparrow\rangle,$$
$$|\downarrow\rangle_h = |S\rangle |\downarrow\rangle,$$

(2.1)

where J_{h} is the total angular momentum of the hole, $|S\rangle$ is the s-symmetry operator and $|\uparrow\rangle, |\downarrow\rangle$ denote spin up and spin down states, respectively.

States in the conduction band are described by three components of the Bloch

function $|X\rangle, |Y\rangle, |Z\rangle$. This, in combination with spin-orbital coupling, results in doubly degenerate total angular momentum of electron $J_\mathrm{e} = \frac{1}{2}$:

$$J_\mathrm{e} = \frac{1}{2} : |\Uparrow\rangle_\mathrm{e} = -\frac{1}{\sqrt{3}} \left[(|X\rangle + \mathrm{i}\,|Y\rangle) \, |\downarrow\rangle + |Z\rangle \, |\uparrow\rangle \right],$$
$$|\Downarrow\rangle_\mathrm{e} = \frac{1}{\sqrt{3}} \left[|Z\rangle \, |\downarrow\rangle - (|X\rangle - \mathrm{i}\,|Y\rangle) \, |\uparrow\rangle \right]. \tag{2.2}$$

The spin-orbital coupling splits the energy level into two and its effect causes the spin is no longer preserved. Instead, the total angular momentum $J = J_\mathrm{h} \pm J_\mathrm{e}$ is preserved. Combining the two states in equations 2.1 and 2.2, we get either $J = 0$ or $J = 1$. For $J = 0$ it is a single state, therefore a singlet

$$|\Psi_{0,0}\rangle = -\frac{1}{\sqrt{2}} \left[|\Downarrow\rangle_\mathrm{e} \, |\uparrow\rangle_\mathrm{h} - |\Uparrow\rangle_\mathrm{e} \, |\downarrow\rangle_\mathrm{h} \right]. \tag{2.3}$$

For $J = 1$ we get three non-degenerate states, i.e., a triplet

$$|\Psi_{1,-1}\rangle = |\Downarrow\rangle_\mathrm{e} \, |\downarrow\rangle_\mathrm{h}\,,$$
$$|\Psi_{1,0}\rangle = -\frac{1}{\sqrt{2}} \left[|\Downarrow\rangle_\mathrm{e} \, |\uparrow\rangle_\mathrm{h} + |\Uparrow\rangle_\mathrm{e} \, |\downarrow\rangle_\mathrm{h} \right], \tag{2.4}$$
$$|\Psi_{1,+1}\rangle = |\Uparrow\rangle_\mathrm{e} \, |\uparrow\rangle_\mathrm{h}\,.$$

Should we calculate the probability of each state we end up with: zero for $J = 0$, suggesting a dark singlet, and non-zero for the triplet, suggesting a bright triplet. Calculating the energy of each state would reveal their theoretical order - the singlet below the triplet.

Now comes the time to mention the other reason for LHPs' unique qualities - the Rashba effect. The Rashba effect causes the momentum-dependent splitting of spin bands. The effect is the consequence of spin-orbital interaction and asymmetrical potential in the crystal. As a result of the Rashba effect, the triplet and the singlet switch places, therefore the bright triplet becomes the ground state [22, 23].

The previously described fine structure has proven to be able to emit 1000 times faster than regular SCs [24]. Each of the three orthogonal non-degenerate states we obtained in equation 2.4 emit as a linear dipole. The radiative lifetime of an exciton is given as

$$\frac{1}{\tau_{ex}} = \frac{4\omega n E_\mathrm{p}}{9 \times 137 m_0 c^2} I_\parallel^2, \tag{2.5}$$

where the important parts are E_p, Kane energy, which is the energy the exciton can emit, and $I_\parallel$, the so-called overlap integral, which contains an envelope function, describing the exciton's confinement [25].

The final order of the energy states in the fine structure is given by the value of Rashba coefficients. Their sign determines whether the helicity is conserved between the top of the valence band and the bottom of the conduction band. Helicity is the projection of the angular momentum vector in the direction of the momentum vector $\mathbf{k}$. The same sign means the helicity is preserved. Given the helicity is preserved, optical

transitions are allowed between such bands [26].

The end product of the article, shown in Figure 2.4, is a set of rules an SC must adhere to have the ability to emit from a ground state bright triplet:

- lack of **inversion symmetry**,

- the edges of the conduction and the valence bands have either **s- or p-symmetry**,

- the band exhibiting p-symmetry must be strongly affected by **spin-orbital coupling**,

- Rashba coefficients for electron and hole are **non-zero** and of the same sign.

As of now, the only SCs known to meet these criteria are LHPs [21].
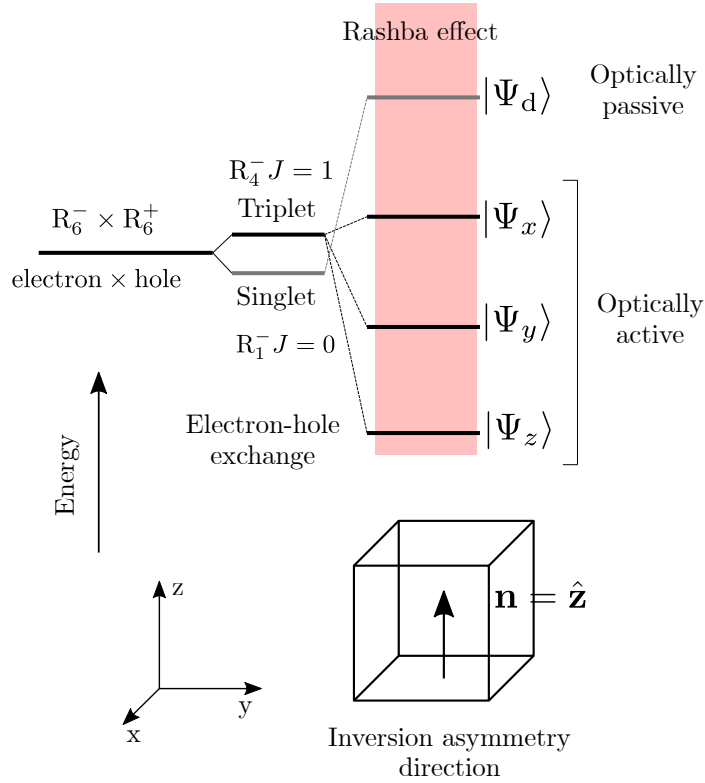
Figure 2.4: Schematic of the energy levels in LHPs. The level is firstly split into a singlet and triplet due to the spin-orbital coupling caused by the presence of heavy metal in the lattice. The Rashba effect affects the final order of the energy levels, resulting in the bright triplet laying beneath the dark singlet state. Adapted and edited from [21].

2.4   Applications

Due to the research and the understanding of their unique qualities, LHPs have enjoyed an enormous rise in popularity over the last decade and have become one of the most sought after materials in optoelectronics.

The best-known use of LHPs in the mainstream is in the field of photovoltaics. The combination of the material's highly tunable band gap and low manufacturing costs make LHPs the ideal candidate for solar cells. Tuning the band gap via change of the halide content in the compound and optimizing it for the solar spectrum increases the material's efficiency [8].

As a material efficient in solar cells LHPs should therefore prove to also be very fine light emitters. LEDs based on LHPs have shown high external quantum efficiencies (EQE). To achieve higher EQE metal doping can be introduced. Another upside of doping is the improvement of thermal and air stability which results in a larger Stokes shift [15, 27].

LHP nanowire (NW) lasers, seen in Figure 2.5, serve as miniaturized light sources which could find their use in many fields. The combination of 1D geometry and high refractive index make for strong quantum confinement. The NWs along their axis serve as the gain medium for light amplification, while the smooth end facets function as Fabry-Perot cavities, triggering light emission. NWs of solution-grown organic-inorganic hybrid perovskites have shown very low lasing thresholds, high Q-factor and broad wavelength tunability (500–820) nm. LHPs have been also studied for use contrariwise to lasers, i.e., for optical limiting. Owing to their two-photon and multiple-photon absorption properties LHPs could function as laser light limiting materials, lowering the possible laser-induced damage to optical devices and even the human eye [28, 29, 30].
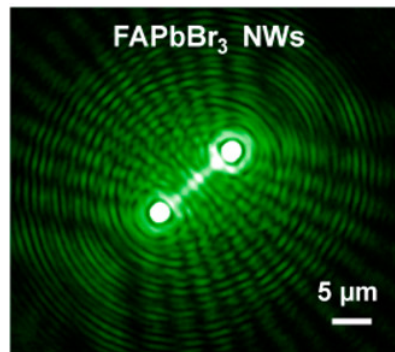
Figure 2.5: Optical image of a green-lasing $FAPbBr_3$ NW. Adapted and editted from [29].

The wide-ranging PL observed in LHPs is highly desirable in display applications. LHPs could very soon find their use in LCD back-lighting as colour-pure red and green emitters. Furthermore, LHPs can serve as colour-controlling and colour-enhancing films in portable devices [31, 32, 27].

3. Density Functional Theory

The density functional theory (DFT) serves as a relatively simple solution to complex many-body problems that arise in solid-state physics, here we shall cover how DFT came to be and how it works.

3.1 Variation method for ground state

The variation method is used for estimating the ground state energy E_0 in quantum mechanics, it is based on the variation principle, see Figure 3.1.

The average energy of a system obtained over many measurements is given by the formula

$$E(\Psi) = \frac{\langle \Psi | \hat{\mathbf{H}} | \Psi \rangle}{\langle \Psi | \Psi \rangle}, \tag{3.1}$$

where $\langle \Psi | \hat{\mathbf{H}} | \Psi \rangle = \int \Psi^* \hat{\mathbf{H}} \Psi \, \mathrm{d}x$. The procedure is as follows, a trial ket $| \Psi \rangle$ is chosen based on experience and its energy $E(\Psi)$ is found using equation 3.1. With each new iteration we obtain new energy values which all meet this criteria

$$E(\Psi) \geqq E_0. \tag{3.2}$$

The energy of the estimated state provides an upper bound in our search for the actual lowest energy E_0. The next step is the minimization of the functional. Accounting for all N-electron wave functions the minimization of the functional will result in finding the ground energy E_0 [3, 33] given by

$$E_0 = \min_{\Psi} E(\Psi). \tag{3.3}$$

Figure 3.1: Variation principle demands the trajectory to be the stationary point of the system. Adapted and edited from [34].

3.2 Approximations and assorted theories of DFT
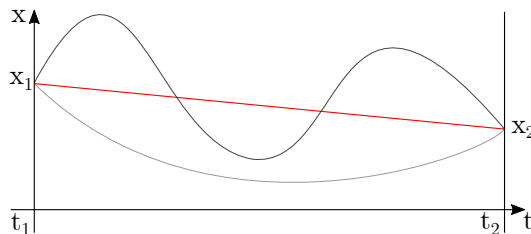
The ability to find the ground state of a quantum system merely by minimizing a functional is of great use in physics. It is the principle upon which the DFT calculations were built, where the functional in question is the electron density functional.

3.2.1 Hohenberg-Kohn theorem

To resolve the problem of solving the SE for realistic, complex systems, Hohenberg and Kohn offered a solution, the basis of which was the electron density as the means to fully describe a given quantum system. They proposed two theorems.

The first theorem states that external potential is completely defined by the electron density $n(\mathbf{r})$, which therefore means the energy of the system is too. In turn, the external potential completely defines the wave function of the ground state, hence this wave function is completely defined by the electron density $n(\mathbf{r})$.

The second theorem states that there is a universal electron density functional $F[n(\mathbf{r})]$, independent of the external potential and the global minimum of this functional is equal to ground-state electron density, therefore we can apply variation principle to find this value.

The first theorem is understood as saying that Ψ is a functional of $n(\mathbf{r})$ and so has to be the kinetic and interaction energy, then we can define

$$F[n(\mathbf{r})] \equiv \langle \Psi | \, \hat{\mathbf{T}} + \hat{\mathbf{U}} \, | \Psi \rangle, \tag{3.4}$$

where $F[n(\mathbf{r})]$ is the sought after universal functional. Using the electron density functional we define the energy functional for a given potential $v(\mathbf{r})$

$$E_{\mathrm{v}}[n(\mathbf{r})] \equiv \int v(\mathbf{r}) n(\mathbf{r}) \, \mathrm{d}\mathbf{r} + F[n], \tag{3.5}$$

which is equal to the ground state considering the correct $n(\mathbf{r})$. For function $n(\mathbf{r})$ to be considered 'correct' it has to fulfill the condition $N[n] = \int n(\mathbf{r}) \, d\mathbf{r} = N$, where N is the number of electrons.

The Hohenberg-Kohn theorems do not however prescribe the form of the universal functional. In practice, it has to be approximated and the most commonly used approximation is based on the Kohn-Sham equations [35, 36].

3.2.2 Kohn-Sham equations

Kohn and Sham built upon the discoveries of Hohenberg and Kohn in their theorem by including in an approximate way the exchange and correlation effects. The equations are a set of non-interacting Schrödinger-like equations of a Kohn-Sham system. The Kohn-Sham system is a fictitious system of non-interactive electrons giving the same density as a system of interacting particles.

The energy of inhomogeneous gas of interacting electrons in a static potential $v(\mathbf{r})$ is expressed as

$$E = \int v(\mathbf{r})n(\mathbf{r})\,\mathrm{d}\mathbf{r} + \frac{1}{2}\iint \frac{n(\mathbf{r})n(\mathbf{r}')}{|\mathbf{r} - \mathbf{r}'|}\,\mathrm{d}\mathbf{r}\,\mathrm{d}\mathbf{r}' + G[n] \qquad (3.6)$$

where $n(\mathbf{r})$ is the density and $G[n]$ is a universal functional of the electron density. We can write the universal functional as

$$G[n] \equiv T_\mathrm{s}[n] + E_\mathrm{xc}[n], \qquad (3.7)$$

where $T_\mathrm{s}[n]$ is the kinetic energy and $E_\mathrm{xc}[n]$ the exchange-correlation energy of the system. $T_\mathrm{s}[n]$ is not known, however it can be expressed using single electron wave functions $|\psi_i(\mathbf{r})\rangle$:

$$T_\mathrm{s}[n] = \sum_i \langle \psi_i(\mathbf{r})| \frac{\nabla^2}{2} |\psi_i(\mathbf{r})\rangle, \qquad (3.8)$$

where $\sum_i |\psi_i(\mathbf{r})|^2 = n$. For slowly varying $n(\mathbf{r})$

$$E_\mathrm{xc}[n] = \int n(\mathbf{r})\varepsilon_\mathrm{xc}[n(\mathbf{r})]\,\mathrm{d}\mathbf{r}, \qquad (3.9)$$

where ε_xc is the exchange-correlation energy of one electron in a uniform electron gas of density n. The approximation lays in assuming the equation 3.9 describes the exchange-correlation effect exactly. Substituting equations 3.7 and 3.9 into 3.6 and solving for minimum we obtain

$$\int \delta n(\mathbf{r}) \left\{ \varphi(\mathbf{r}) + \frac{\delta T_\mathrm{s}[n]}{\delta n(\mathbf{r})} + \mu_\mathrm{xc}[n(\mathbf{r})] \right\} \mathrm{d}\mathbf{r} = 0, \qquad (3.10)$$

under the condition $\int \delta n(\mathbf{r})\,\mathrm{d}\mathbf{r} = 0$, where

$$\varphi(\mathbf{r}) = v(\mathbf{r}) + \int \frac{n(\mathbf{r}')}{|\mathbf{r} - \mathbf{r}'|}\,\mathrm{d}\mathbf{r}', \qquad (3.11)$$

and

$$\mu_\mathrm{xc}[n(\mathbf{r})] = \frac{\mathrm{d}[n\varepsilon_\mathrm{xc}(n)]}{\mathrm{d}n} \qquad (3.12)$$

is the exchange-correlation contribution to the chemical potential.

Seeing as equation 3.11 and its condition are the same as those Hohenberg and Kohn [35] would have obtained for a system of non-interacting electrons in the $\varphi(\mathbf{r})+\mu_\mathrm{xc}[n(\mathbf{r})]$ potential, $n(\mathbf{r})$ can be acquired by solving the so-called Kohn-Sham equation

$$\left\{ -\frac{1}{2}\nabla^2 + \left[\varphi(\mathbf{r}) + \mu_\mathrm{xc}[n(\mathbf{r})] \right] \right\} \psi_i(\mathbf{r}) = \varepsilon_i \psi_i(\mathbf{r}) \qquad (3.13)$$

for given φ and μ, considering

$$n(\mathbf{r}) = \sum_{i=1}^{N} |\psi_i(\mathbf{r})|^2, \qquad (3.14)$$

is the sum of partial densities and N is the number of electrons. The term ε_{xc} in expression 3.12 is not known and therefore has to be approximated, this is expanded upon in the following sections.

3.2.3   Local-density approximation

Local-density approximation (LDA) is an approximation of the exchange-correlation functional used to improve upon Kohn's and Sham's expression of the term in their equations.

Kohn and Sham were the first to attempt to solve the problem of the unsatisfactory exchange-correlation term that has arisen from their previous solutions. The exchange-correlation energy is written as

$$E_{\text{xc}}^{\text{LDA}}[n] = \int n(\mathbf{r})\varepsilon_{\text{xc}}[n(\mathbf{r})]\,\mathrm{d}\mathbf{r}, \tag{3.15}$$

and $\varepsilon_{\text{xc}}(n)$ is the energy per particle in a uniform gas of density n. E_{xc} can be expressed as a linear combination of the exchange and correlation energies as such

$$E_{\text{xc}} = E_{\text{x}} + E_{\text{c}}. \tag{3.16}$$

The exchange functional is based on homogeneous electron gas as its exchange-energy density is known analytically, resulting in

$$E_{\text{x}}^{\text{LDA}}[n] = -\frac{3}{4}\left(\frac{3}{\pi}\right)^{1/3}\int n(\mathbf{r})^{4/3}\,\mathrm{d}\mathbf{r}. \tag{3.17}$$

The correlation functional is known analytically only in high- and low-density limits. In recent years a new correlation functional based on the many-body perturbation theory has been proposed. The most used LDA functionals are based on Quantum Monte Carlo data, which they try to parameterize, for example, the Vosko-Wilk-Nusair (VWN) correlation functional [37].

For situations when spin ought to be taken into consideration the LDA has been modified into LSDA, i.e., local spin density approximation. The terms previously described are expanded for two possible spin polarization. The exchange-correlation energy becomes

$$E_{\text{xc}}[n_{\uparrow}, n_{\downarrow}] = \int n(\mathbf{r})\varepsilon_{\text{xc}}(n_{\uparrow}, n_{\downarrow})\,\mathrm{d}\mathbf{r}, \tag{3.18}$$

where $\varepsilon_{\text{xc}}(n_{\uparrow}, n_{\downarrow})$ is the exchange-correlation energy per electron of an electron gas with uniform spin densities $n_{\uparrow}$ and $n_{\downarrow}$ [3, 38, 39, 40].

3.2.4   Generalized gradient approximation

Even though the introduction and refinement of the LDA method meant a huge stride forward in the accuracy of ab-initio calculations. However, LDA's crux lies in its assumption that the electron density is the same everywhere and thus this method might

fail in the description of such systems where the electron density changes considerably over the space.

As its name suggests the generalized gradient approximation (GGA) considers changes in the density over space by introducing dependence on the gradient of n. The LSDA exchange-correlation term 3.18 subsequently changes as

$$E_{\text{xc}}^{\text{GGA}}[n_\uparrow, n_\downarrow] = \int n(\mathbf{r}) \varepsilon_{\text{xc}}(n_\uparrow, n_\downarrow, \nabla n_\uparrow, \nabla n_\downarrow)\, \mathrm{d}^3\mathbf{r}. \tag{3.19}$$

The GGA leads to an overall improvement of total energies, atomization energies, energy barriers and structural energy differences with respect to LSDA [41, 42].

3.2.5 Hartree-Fock method

The Hartree-Fock method predates the Kohn-Sham DFTs and serves as an alternative approach. There are also the so-called hybrid functionals which combine energies calculated by Hartree-Fock's method with classical DFT. Hartree's approach was to substitute the two-particle interaction term for a single-particle one

$$\frac{1}{2} \sum_{\substack{i,j \\ i \neq j}} \frac{e^2}{|\mathbf{r}_j - \mathbf{r}_i|} \rightarrow U_{\text{ef}}^{\text{H}} = \sum_{i=1}^{N} U_i(\mathbf{r}_i) = \sum_{\substack{j=1 \\ j \neq i}}^{N} e^2 \int \frac{\psi_j^*(\mathbf{r}')\psi_j(\mathbf{r}')}{|\mathbf{r} - \mathbf{r}'|}\, \mathrm{d}^3\mathbf{r}', \tag{3.20}$$

which would serve as an effective potential compensating for the effect of the remaining $(n-1)$ electrons.

Fock built upon Hartree's conclusions by incorporating Pauli's principle. That is achieved by approximating Ψ as an antisymmetrized product of N orthonormal spin orbitals $\psi_i(\mathbf{x})$, the Slater determinant

$$\Psi_{\text{HF}} = \frac{1}{\sqrt{N!}} \begin{vmatrix} \psi_1(\mathbf{x_1}) & \psi_2(\mathbf{x_1}) & \cdots & \psi_N(\mathbf{x_1}) \\ \psi_1(\mathbf{x_2}) & \psi_2(\mathbf{x_2}) & \cdots & \psi_N(\mathbf{x_2}) \\ \vdots & \vdots & \ddots & \vdots \\ \psi_1(\mathbf{x_N}) & \psi_2(\mathbf{x_N}) & \cdots & \psi_N(\mathbf{x_N}) \end{vmatrix} = \frac{1}{\sqrt{N!}} \det[\psi_1 \psi_2 \cdots \psi_N]. \tag{3.21}$$

Consequently, Hartree's effective potential (3.20) is expanded with a new term

$$U_{\text{ef}}^{\text{HF}}(\mathbf{r}) = -e^2 \sum_{\substack{j=1 \\ s=s'}}^{N} \frac{\psi_j(\mathbf{r})}{\psi_i(\mathbf{r})} \int \frac{\psi_j^*(\mathbf{r}')\psi_i(\mathbf{r}')}{|\mathbf{r} - \mathbf{r}'|}\, \mathrm{d}^3\mathbf{r}', \tag{3.22}$$

the $s = s'$ means summation of states with parallel spins. This 'exchange' term is a result of the exclusion principle and the antisymmetry of the wave function.

An electron considered in the Hartree-Fock approximation is not the classical free electron, but instead a quasiparticle, the so-called Hartree-Fock electron (free electron + exchange hole). The Hartree-Fock electron's effective charge is $(-e)$ however its dispersion relation $E(\mathbf{k})$ is different from equation 1.9.

The total energy in the Hartree-Fock approach is calculated as

$$E = \sum_{j=1}^{N} \varepsilon_i - \frac{e^2}{2} \sum_{i,j}^{N} \iint \frac{|\psi_i(\mathbf{r})|^2 |\psi_j(\mathbf{r'})|^2}{|\mathbf{r} - \mathbf{r'}|} \, \mathrm{d}^3\mathbf{r} \, \mathrm{d}^3\mathbf{r'}, \tag{3.23}$$

where the Hartree-Fock parameter ε_i is the negative ionization energy of an electron in single-particle Hartree-Fock state ψ_i [1, 3].

3.3 Pseudo-potential approximation

Many approximations in DFTs are made to save computation time, in order to make the calculations a proficient tool. One such approximation is made by dividing the electrons of an atom into two groups, the inner core and the valence electrons. Further, in many cases, the inner core electrons can be ignored, which effectively creates a system of ions interacting with the valence electrons. The effective interaction is called a pseudo-potential.

Pseudo-potentials approximated in such a way however did not represent reality very well. The modern type of pseudo-potentials was developed to mirror reality. The so-called ab-initio pseudo-potential is obtained by fitting a pseudo-potential to a free-atom SE of a realistic electron configuration, thus creating wavefunctions that will, beyond a certain distance r_c, coincide with the true wave functions, see Figure 3.2 [43, 44, 45].
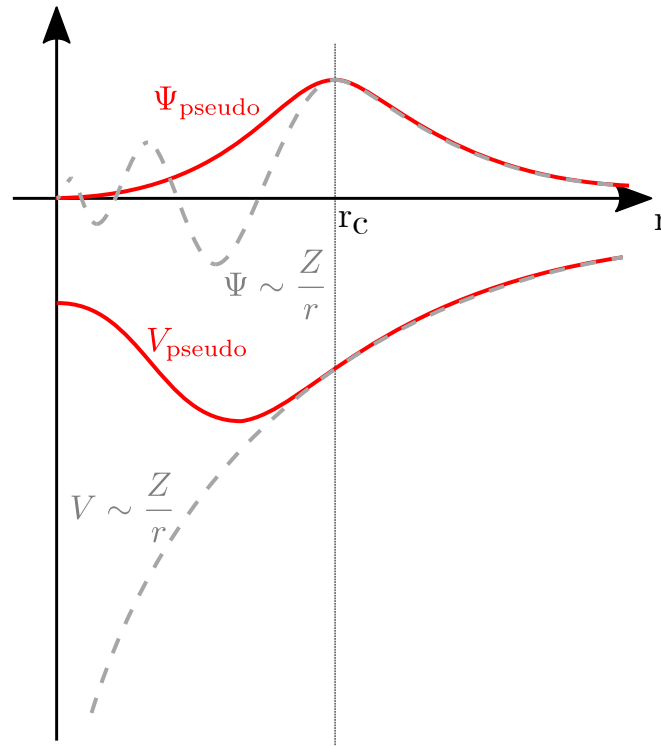

Figure 3.2: Comparison of the real wavefunction and potential (gray) with the approximated 'pseudo' ones (red). We see they match beyond a cut-off radius r_c, the Couloumb radius.

3.4 DFT calculation

DFT calculation begins with an initial guess of the electron density $\rho(\mathbf{r})$, upon which the self-consistent cycle begins. The self-consistent calculation runs until convergence is reached or until the maximum number of steps has been made. Convergence with requested accuracy is reached once the difference in the ground state energy between the previous and current step fulfils the condition $\Delta E < E_{\mathrm{CUT}}$, where E_{CUT} is the energy limit specified by the user according to their needs.

Initial guess
$\rho(\mathbf{r})$

Calculate effective potential
$$v_{\mathrm{eff}}(\mathbf{r}) = V_{\mathrm{en}}(\mathbf{r}) + \int \frac{\rho(\mathbf{r}')}{|\mathbf{r}-\mathbf{r}'|}\,\mathrm{d}\mathbf{r}' + V_{\mathrm{xc}}[\rho(\mathbf{r})]$$

Solve Kohn-Sham equations
$$\left[-\frac{\hbar^2}{2m_{\mathrm{e}}}\nabla_i^2 + v_{\mathrm{eff}} \right]\Psi_i = \varepsilon_i \Psi_i$$

Evaluate the electon density & total energy
$$\rho(\mathbf{r}) = \sum_i |\Psi_i(\mathbf{r})|^2 \rightarrow E_{\mathrm{tot}}[\rho(\mathbf{r})] = \cdots$$

no — Converged?

yes

Output quantities
$\rho_0(\mathbf{r}), E_i[\rho_0(\mathbf{r})] \rightarrow \mathrm{Forces}, \mathrm{Eigenvalues}$
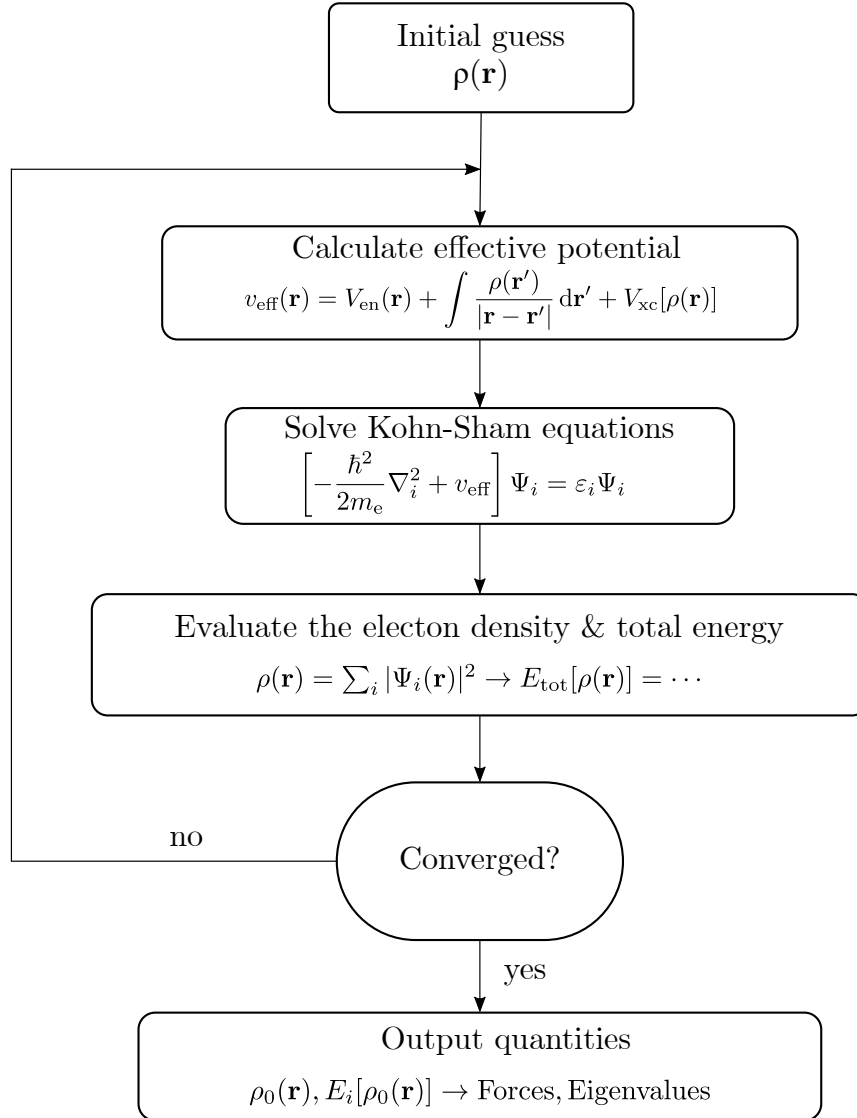
Figure 3.3: Schematic describing the process of a DFT calculation. An initial guess of the electron density serves as the input, which is used in the construction of the effective potential. This is followed by the assembly of and solution of the Kohn-Sham equations. The result is a new electron density, from which the total energy can be calculated. If the total energies of the last two steps differ less than a given constant we say the calculation has converged and we can obtain the sought after resulting values. If the convergence was not reached the calculation restarts with the result electron density. Adapted and edited from [46].

Input files

For our calculations we use the Vienna Ab-initio Simulation Package (VASP) [47, 48, 49, 50]. Calculation in VASP requires four input files, each providing specific information important to the process. The detailed input and output files can be found in Appendix A.

- `POSCAR` is the file specifying the lattice geometry and ionic positions of the crystal in question. The structure used in our calculations looks as follows

```
CsPbBr3
   5.92
     1.0200333401049706     0.0000000000000000     0.0000000000000000
     0.0000000000000000     1.0200333401049706     0.0000000000000000
     0.0000000000000000     0.0000000000000000     1.0200333401049706
   Cs   Pb   Br
    1    1    3
Direct
  0.0000000000000000  0.0000000000000000  0.0000000000000000
  0.5000000000000000  0.5000000000000000  0.5000000000000000
  0.5000000000000000  0.5000000000000000  0.0000000000000000
  0.0000000000000000  0.5000000000000000  0.5000000000000000
  0.5000000000000000  0.0000000000000000  0.5000000000000000
```

- The `POTCAR` file contains all information about the pseudopotential for a given element, as well as the basic information about the atom. This file is generated directly in VASP as the program provides several types of pseudopotentials. When generating the `POTCAR` file it is important to keep the order of elements set in the `POSCAR` file on the sixth line.

- In the `KPOINTS` file we find the sampling of the reciprocal lattice. Depending on the type of calculations there are several types of k-point sampling.

- The `INCAR` file is where we define the parameters of the calculation itself [51].

Output files

VASP produces a great number of output files, many of which find their use only in very specific situations, however, we present a handful of files that are useful in most calculations.

- `CHGCAR` contains the final lattice vectors, atomic positions and the charge density multiplied by volume. It can also be used as an input file to start a calculation from precalculated charge density (`ICHARG = 1`).

- `CONTCAR` has the same format as `POSCAR` and contains the configuration of the system after each ionic step. It is the main product of relaxation calculations, serving as the 'relaxed' `POSCAR` for further runs.

- `EIGENVAL` stores the Kohn-Sham eigenvalues for each k-point at the end of the calculation.

- `OUTCAR` presents a complete output of a given DFT calculation, such as information about the electronic steps, stress tensors or forces on the atoms.

- `WAVECAR` holds the predicted wave function in the form of plane waves in the case of dynamic calculations or the solution to the Kohn-Sham equations after the last step when static or relaxation calculations are concerned. `WAVECAR` is often used as a starting file for continuation runs.

Lastly, it is also good to mention `vasprun.xml`, which is a file containing all the previously mentioned information in *xml* form used in post-processing [51].

4. Crystal Structure Optimization of CsPbBr$_3$

Using all the knowledge presented in the previous chapter we embark on the journey to calculate a CsPbBr$_3$ band structure and DOS consistent with experimental data using the DFT method.

Before any calculations can begin we need a well relaxed `POSCAR` file, which means each atom of the CsPbBr$_3$ structure in Figure 4.1 lies in the minimum of the potential encapsulating it. We achieve relaxation in two steps, using molecular dynamics.
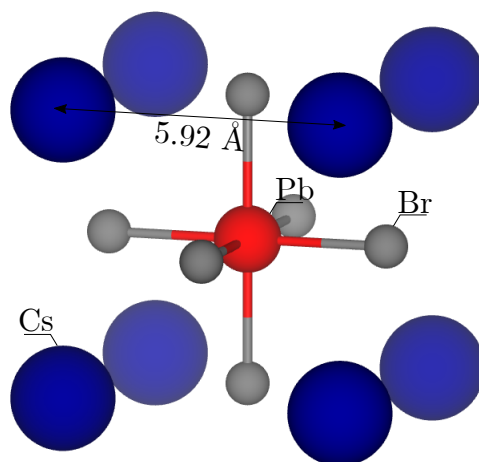

Figure 4.1: Visualisation of the used POSCAR file with $a = 5.92$ Å. Made in VESTA [13].

As we were looking to compare the results of our calculations with experimental data it was good to also start from experimentally obtained data. The initial guess of the lattice constant was therefore made from Transmission Electron Microscope (TEM) measurements of CsPbBr$_3$ crystals, provided by Ing. Michal Horák, PhD, seen in Figure 4.2. We conducted a 2D Fourier transform for each of the chosen crystals, thus obtaining diffraction spectra. from which we were able to measure the distance between the Cs atoms. We calculated the desired lattice constant by fitting the histogram with the normal distribution, see Figure 4.3a and extracted the ideal value of the experimental lattice constant $a = (5.9 \pm 0.2)$ Å with 95% confidence interval.

The first step of the relaxation requires us to find the correct number of plane waves that are to be used to construct the solution to the Kohn-Sham equations. It is crucial to include enough plane waves so that the calculation can converge, however

unnecessarily large quantities of plane waves cause the calculation time to increase significantly very fast. Therefore we have to find the correct balance between these two factors.

The amount of plane waves used is determined by the cut-off energy E_{CUT}, which is in the calculations specified via the `ENCUT` tag. When the correct `ENCUT` is found we also test convergence for different k-point grids. The convergence is checked by comparing the free energy per one atom between each step, when the difference reached the set limit of 1 meV we would deem the given parameter correct, as the changes in the free energy per one atom were not significant enough to interfere with the calculated structure. The resulting values were 400 eV as the plane wave energy cut off and $6 \times 6 \times 6$ k-point grid.

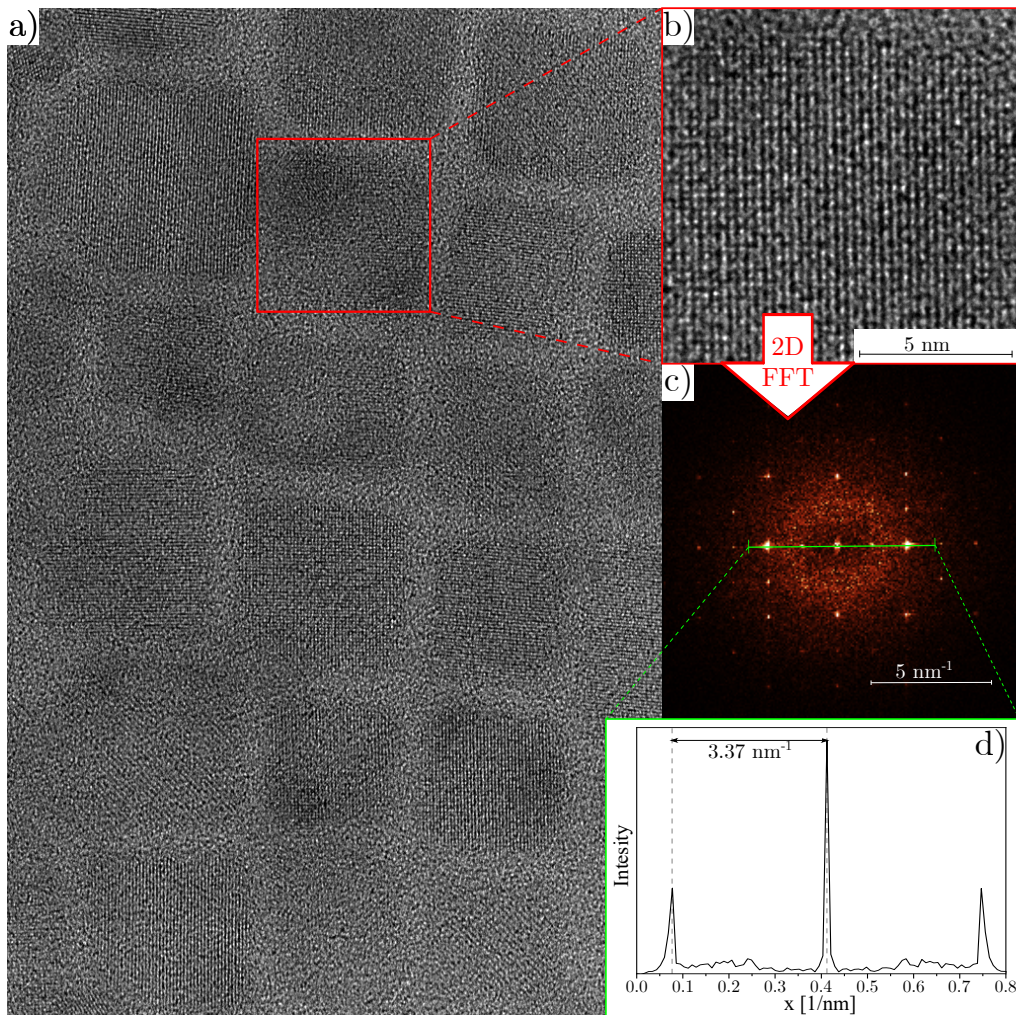**Figure 4.2:** a) Thanks to Ing. Michal Horák, PhD, we obtained a TEM image of an array of CsPbBr$_3$ crystals. b) Using Gwyddion [52] we singled out a crystal and c) using the 2D Fast Fourier Transform tool we obtained a diffraction pattern. d) By measuring the distance between the maxima (Cs atoms) we found a reciprocal value of $2a$. Solving for a we found a lattice constant for the examined crystal.

In the second step comes volume relaxation, which is done by finding the volume with minimal free energy. The value obtained from the TEM data now served as the basis of our relaxation calculations. We ran optimization calculations at fixed volumes using structures with lattice parameters with $\pm 7\%$ deviation from the measured value, meaning (5.9 ± 0.4) Å, and acquired a graph showing cell volume's dependence on free energy, shown in Figure 4.3b.
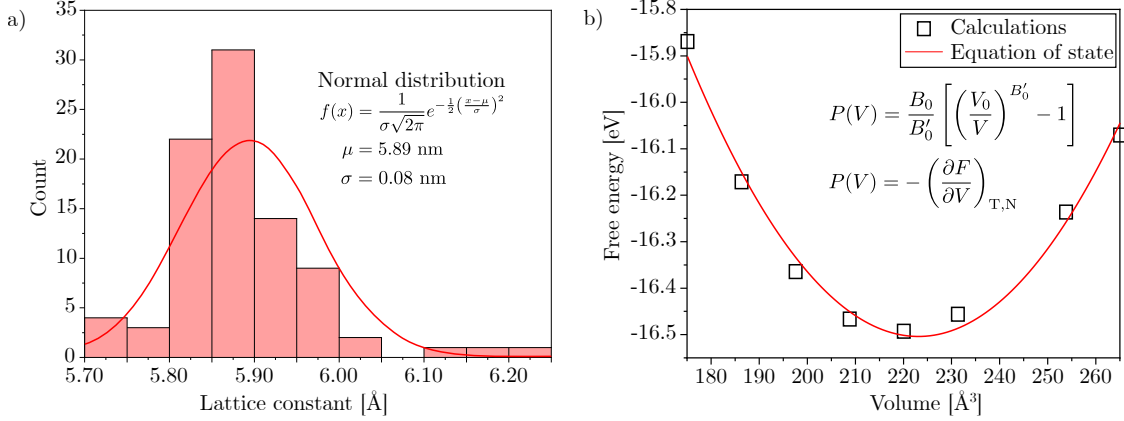

Figure 4.3: a) We measured 40 crystals and obtained a statistic shown in the histogram. Fitting the data with the normal distribution we obtained the experimental lattice constant to be $a_e = (5.9 \pm 0.2)$ Å. b) Conducting molecular dynamics calculation in an interval of lattice parameters around 5.9 Å we obtained values of free energy for each parameter. Fitting these points with the Murnaghan equation of state results in the ideal lattice parameter of $a_i = 5.92$ Å.

Free energy and cell volume were read from the `OUTCAR` files of each sub-calculations. The data was fitted by an equation of states as seen in Figure 4.3 using a code adapted from [53]. The fit is a parabolic approximation of the Murnaghan equation of state and the results of the fit are parameters of the equation of states. The bulk modulus of our calculated $CsPbBr_3$ crystal, using the PBE functional, is $B = 20.28$ GPa, and the cohesive energy of the bulk is $E_{coh} = -4.13$ eV. The experimental values are $B = 21.00$ GPa and $E_{coh} = -3.37$ eV [54, 55]. The notable difference between the experimental and calculated value of the cohesive energy is likely due to the use of different functionals in the underlying DFT calculations. The minimum of the parabola and thus the ideal lattice constant lays at $a_i = 5.92$ Å. For the relaxed structure see Figure 4.1.

At the end of the process we run a self-consistent calculation, which means we set the number of ionic steps to zero (`NSW = 0`), using the `POSCAR` file for a_i. The goal of this step was to produce the charge density and set of plane waves which will be used to restart our future calculations.

5. Electronic Structure Calculation of CsPbBr$_3$

In this chapter, we venture to calculate the band structure, DOS and effective mass of a CsPbBr$_3$ bulk, which we will compare to experimentally acquired data in the next chapter to assess our ability to reach relevant results using the DFT method.

CsPbBr$_3$'s unique structure poses a challenge for the classical DFT calculations. The presence of the heavy metal, lead, in the structure introduces the effect of spin-orbital coupling into the mix which then has to be accounted for in the actual calculation. Therefore we are required to calculate with great fidelity all the electron orbitals in the atoms of lead, which makes for an expensive calculation, time-wise as well as calculation capacity-wise. To simplify the process somewhat we opted to approximate the realistic orthorhombic structure of CsPbBr$_3$ with a simple cubic lattice.

Throughout this chapter we will often use the term 'classical DFT', by that we mean a DFT calculation employing the most widely used functional, the Perdew–Burke-Ernzerhof (PBE) functional [56, 57]. The PBE functional was created as an improvement upon the LSDA by introducing further physical constraints on the exchange-correlation term. Its popularity lies in its easy convergence and universality of application. It produces good results in band structure calculations, however, it does not bode well when predicting the value of band gap. The PBE's biggest problem is the underestimation of the band gap due to the prioritization of occupied states [58, 59, 60]. All the calculations presented in this thesis were calculated using the projector augmented wave (PAW) pseudopotential [61, 62].

Seeing as CsPbBr$_3$ is no trivial structure and we were just at the beginning of our journey with DFT calculations we approached the task in stages. For the input files see Appendix A. The very first milestone would be correctly implementing the spin-orbit coupling effect into the classical DFT calculation. Both the band structure and DOS calculations were done in two steps. The first, shared step was an accurate self-consistent (SC) collinear calculation in the ground state (using the `vasp_std` package). This was done to 'pre-converge' the calculation, obtaining a set of wave functions in the `WAVECAR` file and a charge density distribution in the `CHGCAR` file.

Due to the inclusion of the spin-orbital coupling, the second step was run as a non-self-consistent (NSC) non-collinear calculation and required the use of `vasp_ncl` package. It was restarted from the set of wave functions a charge density we generated in the first step. The second step serves as either the band structure calculation or DOS calculation thus calling for the NSC approach. The NSC calculation does not start the

next step from the previous one's electron density, but rather runs each step separately from the others. It is used in non-stationary problems, such as the band structure calculation. The NSC of the calculation is implemented by adding 10 to the value of the `ICHARG` tag, here we used `ICHARG = 11`, saying to the program 'start calculation in a non-self-consistent manner, reading the charge density from an existing `CHGCAR` file'.

The DOS calculation requires the use of the tetrahedron smearing method for increased accuracy. The `DOSCAR` file needed during the post-processing is generated thanks to the `LORBIT` tag, through which we can determine how the program calculates the orbitals. We opted for `LORBIT = 10` which results in data split into s, p, d orbitals and thus allows us to calculate projected DOS for those orbitals.

The band structure calculation does not necessitate the change in smearing. What differentiates this calculation is the change in the sampling of the k-point grid in the `KPOINTS` file, the new `KPOINTS` include the coordinates of the high-symmetry points in the first Brillouin zone and a number of intersections, determining how many times the first Brillouin zone will be traced. The calculation was conducted using a simple cubic lattice in an effort to simplify the calculation, see Figure 5.1.
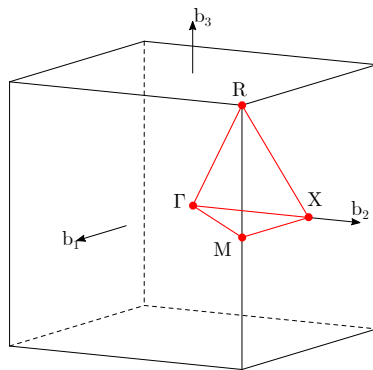

Figure 5.1: The first Brillouin zone of the simple cubic lattice with the points of high symmetry. The path describing the simple cubic lattice is Γ-X-M-Γ-R-X|M-R.

In both second steps, we used the `CHGCAR` and `WAVECAR` from step one and started from pre-converged wave functions and charge density. The calculated band structure and DOS of $CsPbBr_3$ with the effect of the spin-orbital coupling is shown in Figure 5.2. The calculations were processed using `vaspkit` [63] and plotted in OriginPro.

Figure 5.2 shows that the optical transition happens at the R point in the first Brillouin zone of the simple cubic lattice. The difference between the valence band maximum and the conduction band minimum at that point is $E_{\mathrm{CBM}} - E_{\mathrm{VBM}} = 0.77$ eV, resulting in the band gap of the same value. Comparing the outcome with the experimentally obtained value $E_{\mathrm{g}} = 2.36$ eV we see the calculation is severely lacking. The unsatisfactory result was however to be expected as it is well known the PBE functional used in this calculation underestimates the band gap [60]. The effect of the spin-orbital coupling also contributed to the narrower result.

To show the effect spin-orbital coupling has on the energy bands we present a side-by-side comparison of calculated $CsPbBr_3$ structures with the spin-orbital coupling effect turned off and on, see Figure 5.3. The first and the most significant effect spin-orbital coupling has on the calculation is a massive reduction of the band gap. In our
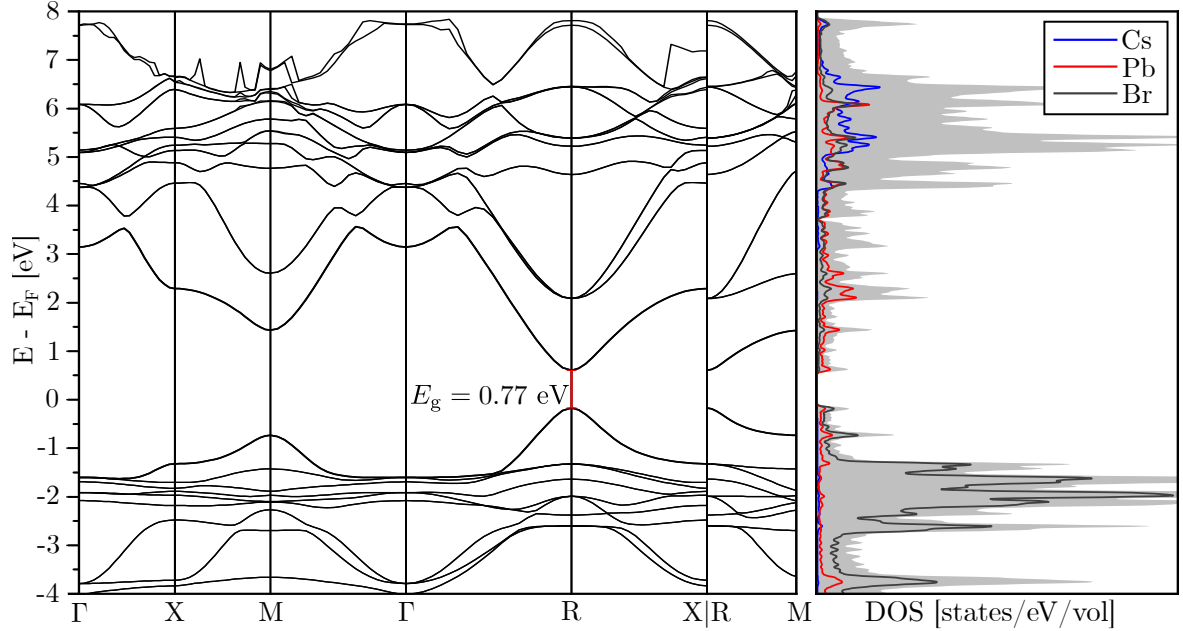
Figure 5.2: Band structure and DOS with spin-orbital coupling: on the left is the band structure graph showing the energy level in relation to the position in the first Brillouin zone. The optical transition happens at the R high-symmetry point. The value of the band gap is $E_g = 0.77$ eV. On the right is the DOS in relation to energy. We see the maximum of the valence band consists of Pb and Br orbitals, and the minimum of the conduction band is mainly characterized by the Pb orbitals, which is in agreement with findings in [21].

case, we observed a decrease by 1.08 eV. The other effect we registered, which is closely related to the band gap reduction, was the splitting of the triply degenerate conduction band minimum. Due to the inclusion of the spin-orbital coupling effect, we obtained a new distribution of the levels. We ended up with a fourfold degenerate state at the conduction band minimum and a twofold split-off level. The lower band represents the electronic spin states $\left| J = \frac{3}{2}, J_z = \pm \frac{3}{2} \right\rangle$, while the higher-energy band represents $\left| J = \frac{3}{2}, J_z = \pm \frac{1}{2} \right\rangle$ [20].

In an effort to improve the value of the band gap we chose to employ the use of hybrid functionals. The HSE type hybrid functional which we chose to use combines the local contribution from Hartree-Fock's exact exchange with the exchange-correlation energy calculated by the PBE functional for the area further from the atom, where it agrees well with reality. What this approach does to the calculated structure is it effectively shifts the unoccupied states higher thus broadening the band gap.

The first hybrid functional we used was the HSE06 functional which includes 25 % mixing of the Hartree-Fock contribution. We carried out the hybrid functional calculation in two steps. The first step was identical to the first step of the previous calculation. Pre-converging the calculation first using the regular PBE functional is the recommended approach as it drastically cuts down the calculation time. The `WAVECAR` and `CHGCAR` files from the first step once again serve as the input of the second step. The form of the DOS and band structure calculations was very similar to the previous calculation.

The hybrid calculation of the band structure implements tags specifying the para-
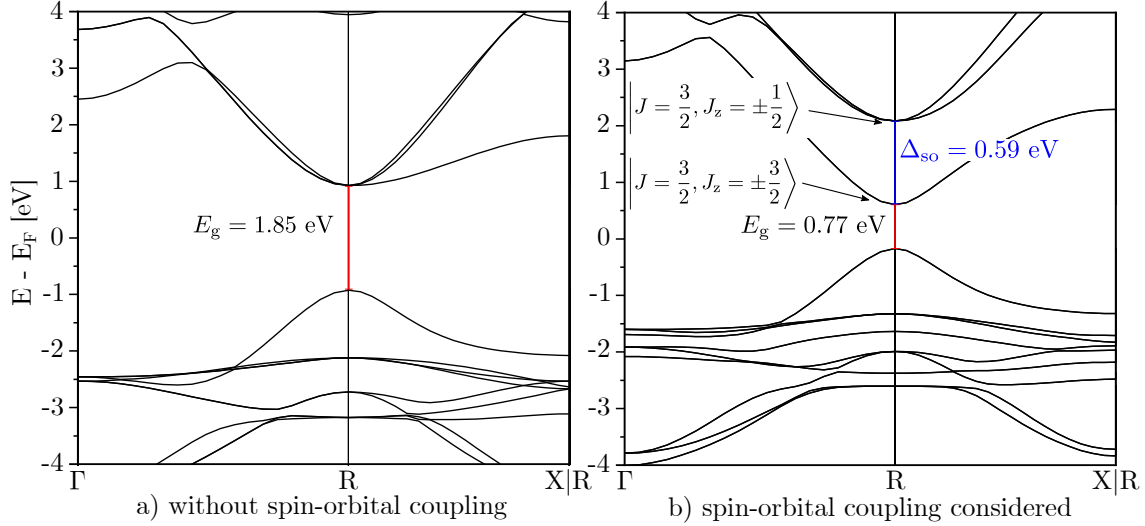
Figure 5.3: Side-by-side comparison of CsPbBr$_3$ band structure calculated using the PBE functional with the spin-orbital coupling effect a) turned off and b) turned on.

meters of the hybrid functional we use. It also requires a suitably modified `KPOINTS` file with a changed sampling of the reciprocal space. The `KPOINTS` file includes the explicit k-points combined with the k-points describing the bulk itself. Those are signified by the 0 weight at the end of the line and are combined with the k-points generated into the `IBZKPT` file. The result of the hybrid calculation using the HSE06 hybrid functional is in Figure 5.4.
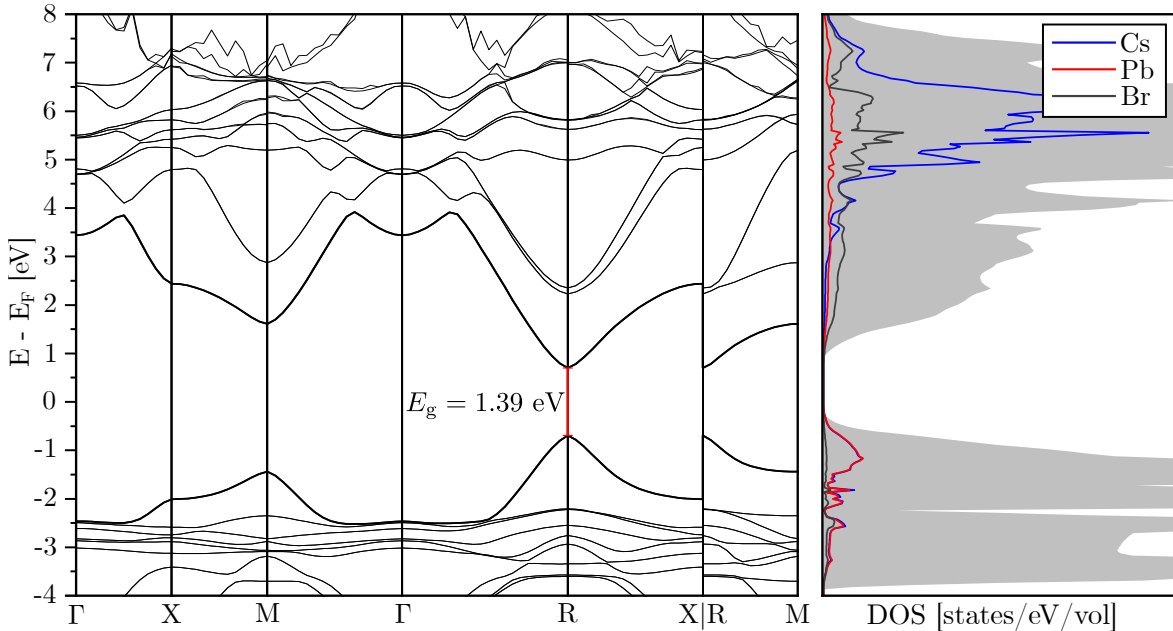

Figure 5.4: Band structure and DOS calculated with HSE06 hybrid functional: on the left is the band structure graph showing energy level in relation to the position in the first Brillouin zone. The optical transition happens at the R high-symmetry point. The value of the band gap is $E_g = 1.39$ eV. On the right is the DOS in relation to energy.

The width of the band gap $E_\mathrm{g} = 1.39$ eV was still unsatisfactory, which led us to increase the mixing of the exact exchange from the Hartree-Fock method as suggested in [21]. The resulting mixing was 45% and it was achieved by adjusting the `AEXX` tag which specifies the fraction of the exact exchange used in a Hartree-Fock type hybrid functional. The resulting structure is in Figure 5.5.
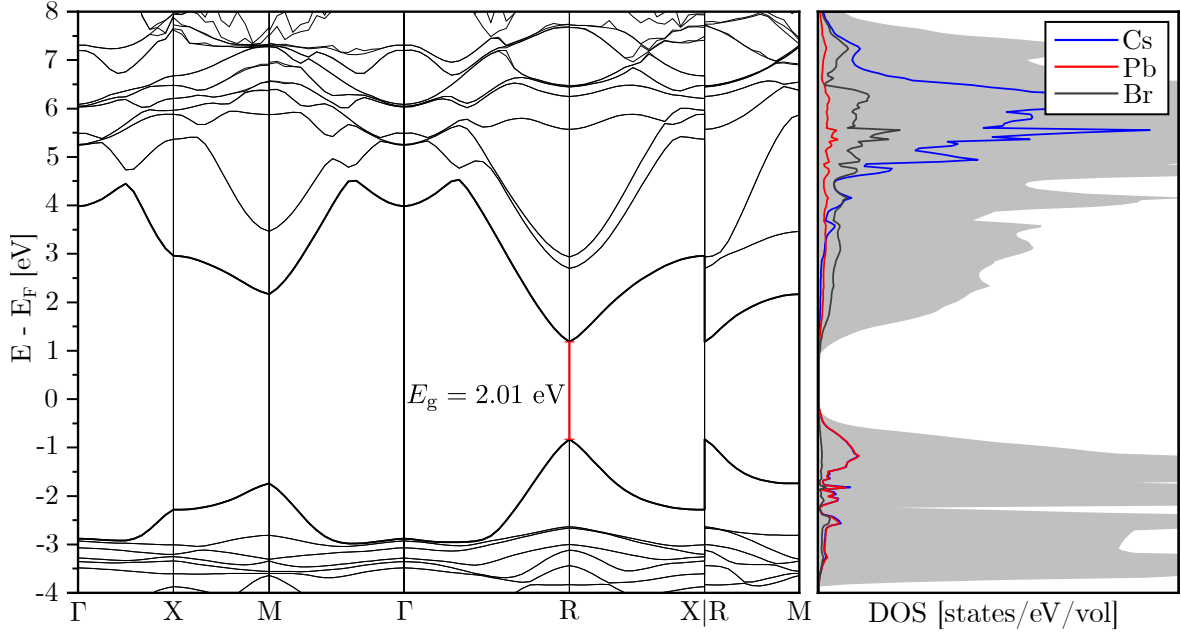

Figure 5.5: Band structure and DOS calculated with 45 % mixing hybrid functional: on the left is the band structure graph showing energy level in relation to the position in the first Brillouin zone. The optical transition happens at the R high-symmetry point. The value of the band gap is $E_\mathrm{g} = 2.01$ eV. On the right is the DOS in relation to energy.

The band gap resulting from this calculation was $E_\mathrm{g} = 2.01$ eV. The value we were attempting to reach was $E_\mathrm{g} = 2.36$ eV. Further mixing of the exact exchange was inadvisable and therefore we opted to implement the scissor operator as suggested in [21].

The scissor operator is a method used to correct the band gap obtained from DFT calculations. The method works by adding a constant term Δ to the energies above the band gap, meaning E_g^{LDA} becomes $E_\mathrm{g}^{LDA} + \Delta_\mathrm{s}$. The value of Δ_s is chosen to correct the calculated band gap to the fundamental gap, it may be set either empirically from the experimental absorption spectra, or one-time higher level generalized Kohn-Sham DFT calculation, e.g. from the GW calculation. Then the value of Δ is obtained as $\Delta = E_\mathrm{g}^{GW} - E_\mathrm{g}^{LDA}$ [64, 65, 66]. The GW calculations utilize the Green function G and the screened Coulomb interaction W, for further information on the subject, see [67, 68]. This approach does however not fall in the category of DFT and is far beyond the scope of this thesis, therefore it was not employed.

Consequently, we have decided for the use of empirical value to set the scissor operator. The experimental value of band gap of $CsPbBr_3$ crystals measured by Ing. Petr Liška is $E_\mathrm{g} = 2.36$ eV. The value of the scissor operator was set to $\Delta_\mathrm{s} = 0.35$ eV to bridge the remaining difference between our biggest calculated band gap $E_\mathrm{g} = 2.01$ eV

and the experimentally acquired value. The band structure with the corrected band gap is in Figure 5.6.
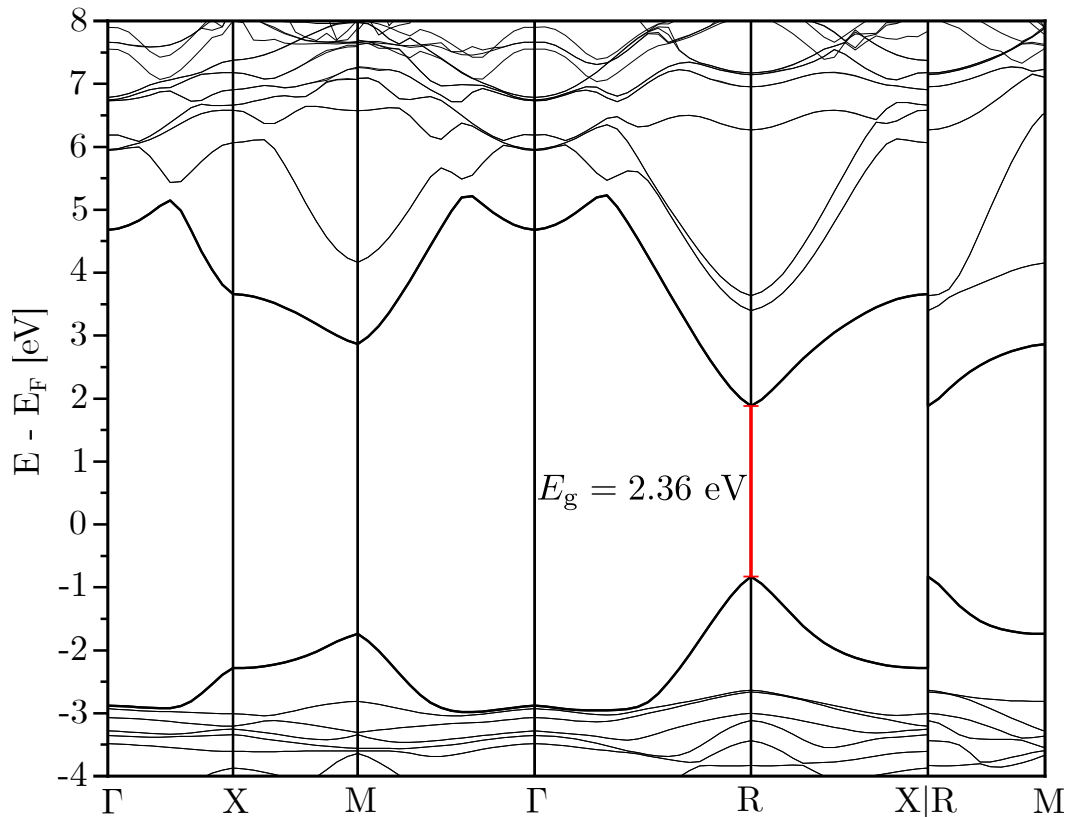
Figure 5.6: Band structure with the scissor operator implemented.

During the post-processing of the data, we were also able to calculate the hole's and electron's effective masses directly in `vaspkit`. Their values will be important in the next chapter, however, in the band structure calculations they served as a fact check for us to ensure the attempts to correct the value of the band gap do not negatively affect the physics of the bands. The effective masses in the Γ–R region from the individual calculations are in Table 5.1 along with their respective value of the band gap.

The fact that the changes in the effective mass with increasing Hartree-Fock mixing are minimal means we can be assured that the physics of the bands remains intact.

Table 5.1: Table comparing the values of bang gap and electron and hole effective masses with experimentally obtained data.

Calculation	E_g $[eV]$	m_e^* $[m_\text{e}]$	m_h^* $[m_\text{e}]$
S–O	0.77	0.177	-0.187
25 %	1.39	0.251	-0.268
45 %	2.01	0.279	-0.289
Experiment	2.36	–	–

6. The Effective Mass Model

In the previous chapter, we have obtained some optical characteristics and electron structure of bulk CsPbBr$_3$ via DFT calculations and in this chapter, we want to compare said results with experimental data. However in reality we study nanostructures of CsPbBr$_3$ as they exhibit enhanced physical and functional properties compared to bulk. Let us consider a quantum mechanical model of an exciton in a finite potential well of arbitrary shape. The model utilizes a single-band effective-mass approximation of the Schrödinger equation to calculate the exciton energy levels, which are used to study the dependence of the PL emission peak energy on the nanocrystal's size, and shape.

We have observed two main groups of the CsPbBr$_3$ nanocrystal shapes as seen in Figure 6.1. The shapes were a lens shape and a triangular shape and we then approximated the given crystals by a corresponding quantum well. Combining the SEM and AFM measurements shown in Figure 6.1 we have acquired the volumetric parameters of said quantum wells. These two techniques need to be combined due to AFM's inability to correctly measure the horizontal dimensions of nanocrystals. The resulting image is a convolution of the sample's topography and AFM's tip. This is where the SEM data play a crucial role, combined with the height profile from AFM we obtain the true 3D model of each nanocrystal.

In Figure 6.2a and b we see two PL maps corresponding to the nanocrystals displayed in Figure 6.1. From these PL maps, we obtained the integral intensity and peak emission wavelength of PL, from which we then calculated the emission energy $E = hc/\lambda$ which we shall compare with the theoretical model. The integral intensity of the PL map (Figure 6.2a) is the area under the curve of intensity in relation to wavelength and it determines the wavelength-weighed power emitted by a crystal via PL, see Figure 6.2c. The emission peak energy is the wavelength corresponding to the position of the centre of mass of the area under the curves in 6.2b, in general, the value of the emission peak energy was $\lambda_0 \sim 520$ nm. In Figure 6.2d we see the PL spectra of two selected nanocrystals one triangular and one with a lens shape

In the approximation, we use the Hamiltonian written as

$$\hat{\mathbf{H}} = -\frac{\hbar^2}{2}\nabla\frac{1}{m^*(x,y,z)}\nabla + V(x,y,z), \qquad (6.1)$$

where m^* is the effective mass of the charge carriers in the crystal and V is the potential field where
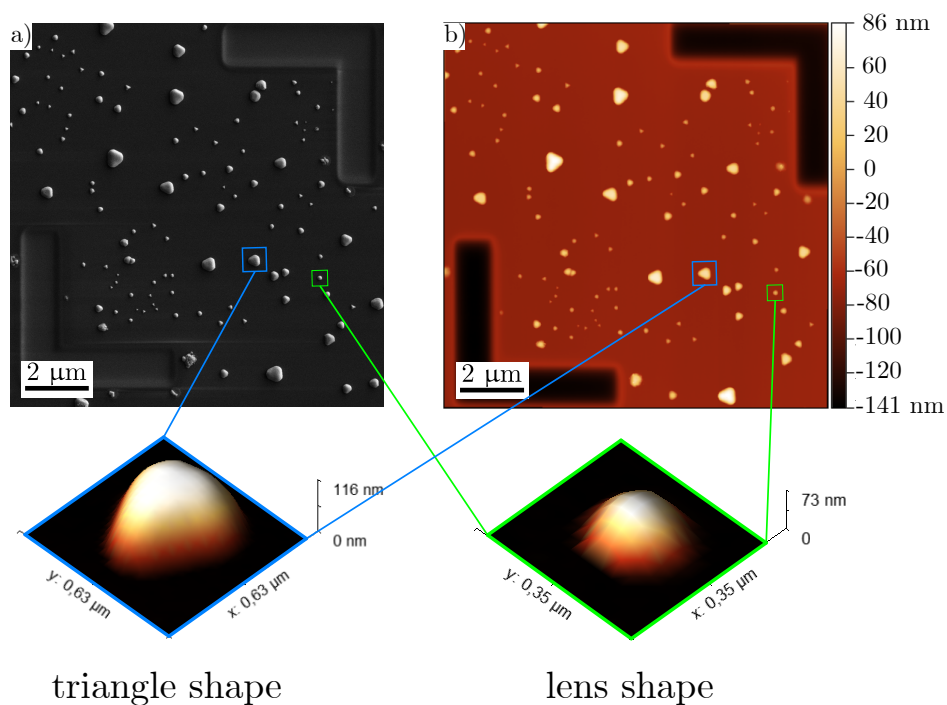
Figure 6.1: We observed two types of shapes of the CsPbBr$_3$ nanocrystals – triangle shape and lens shape. Using the a) SEM and b) AFM measurements we obtained the volumetric parameters of the observed nanocrystals. Processed in Gwyddion [52].
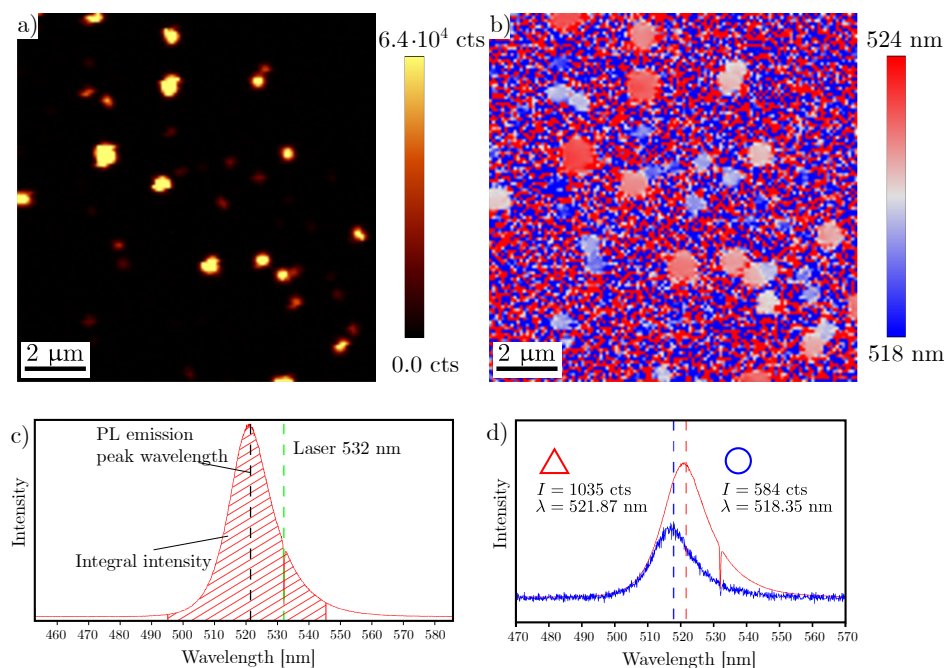
Figure 6.2: From the PL data we were able to acquire the values of a) PL integral intensity and b) PL emission peak wavelength. c) The integral intensity is the area under the curve of intensity in relation to wavelength. d) Two typical spectra of selected nanocrystals. Processed in Gwyddion [52].

$$V(x,y,z) = \begin{cases} 0, & \text{in crystal,} \\ \Delta E_{\mathrm{V}} \text{ or } \Delta E_{\mathrm{C}}, & \text{elsewhere.} \end{cases} \tag{6.2}$$

ΔE_{V} and ΔE_{C} are the valence and conduction band discontinuities, respectively. The wave function is assumed as an expansion of normalized plane waves as follows

$$\psi(x,y,z) = \frac{1}{\sqrt{L_x L_y L_z}} \sum_{nx,ny,nz} a_{nx,ny,nz} e^{\mathrm{i}(k_{nx}x + k_{ny}y + k_{nz}z)}, \tag{6.3}$$

where L_i is the length of the unit cell along the given axis and $k_{ni} = k_i + n_i K_i$, $K_i = 2\pi/L_i$, for $i = x,y,z$; nx,ny,nz give the numbers of plane waves in each direction.

For the triangular shape, the x and y wave functions are inseparable, hence the ground state energy is written as

$$E_{0,xy} = \frac{2h^2}{3ma^2}, \tag{6.4}$$

where a is the edge of the triangular base. The term in z direction takes from of

$$E_{0,z} = \frac{h^2}{8ml_z^2}, \tag{6.5}$$

where l_z is the height of the shape. The two terms are then simply added to form the total ground state energy as follows

$$E_0 = E_{0,xy} + E_{0,z} = \frac{h^2}{m}\left(\frac{2}{3a^2} + \frac{1}{8l_z^2}\right). \tag{6.6}$$

We obtain the term for the total energy of emission from a triangular triangle shaped crystal as

$$E = E_{\mathrm{g}} + \frac{h^2}{\mu}\left(\frac{2}{3a^2} + \frac{1}{8l_z^2}\right), \tag{6.7}$$

where the E_0 term constitutes the quantum confinement contribution and $\frac{1}{\mu} = \frac{1}{m_{\mathrm{h}}^*} + \frac{1}{m_{\mathrm{e}}^*}$ is the reduced effective mass of the exciton. This approach however is not possible with the lens shape as the wave functions for x,y,z are inseparable, from [69] we used the following equation

$$E = E_{\mathrm{g}} + \frac{h^2}{8\mu} V_0^{-2/3}\left(AR^{-4/3} + 2AR^{2/3}\right), \tag{6.8}$$

where μ is the reduced effective mass of the exciton and $AR = l_z/r$ is the aspect ratio of the shape's height and radius, with constant volume $V_0 = 1/6\pi l_z(3r^2 + l_z^2)$.

Now we can compare the calculated PL emission peak energy with the experimentally obtained data. Two such comparisons are in Figures 6.3a and 6.3b, the approximations were made with lens shape and triangular shape, respectively, as they are defined above.

As we can see in Figure 6.3b the crystals approximated by the triangular shape show practically no agreement with the theory. That was however to be expected
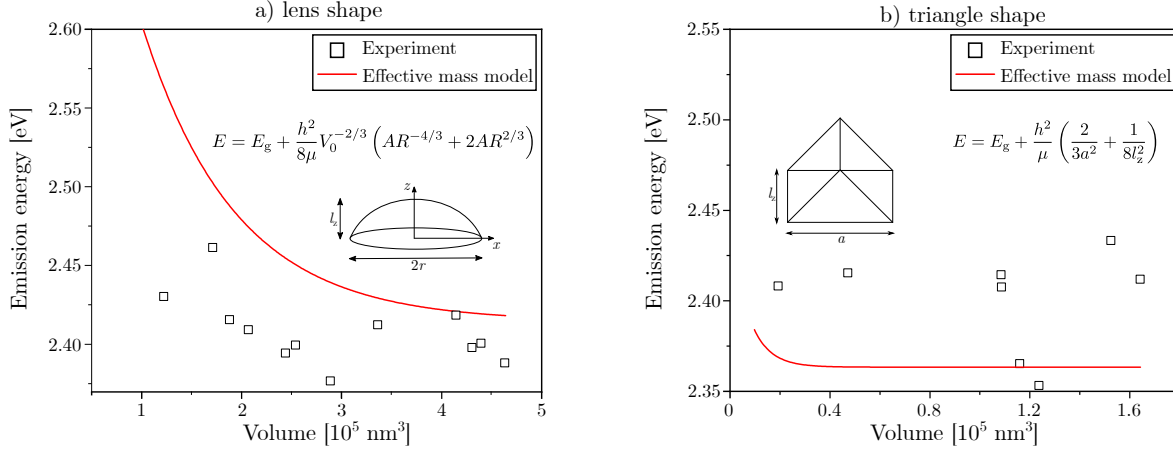
Figure 6.3: We have used the two presented models and fitted the experimental data with the theoretical curve. a) Shows the crystals approximated by a lens shape. The data show a trend consistent with theory as well as the energy values for larger crystals due to favourable noise-to-signal ratio at larger crystal sizes. b) Shows the crystals approximated by the triangular shapes. The theory and experiment show virtually no agreement. It is due to the small size of the crystals, where even a small error in wavelength is projected as a large error in the calculated emission peak energy. And also due to the small crystals' forming in close proximity to one another, the observed emission peak wavelength is negatively impacted.

as all the crystals that could be considered for this approximation were considerably smaller than the lens shapes. Their size and the fact that they often are grouped close together meant low PL emission, and therefore even a small error in the reading of the emission peak wavelength results in a significant discrepancy in the calculated emission peak energy.

The lens-shaped crystals and their corresponding experimental data are plotted in Figure 6.3a. Here we see that the experimental data not only show the same trend as the theoretical curve but it also exhibits some agreement to the energy values, mostly for larger crystals, as for those the noise-to-signal ratio is far more favourable.

The model using lens-shaped crystals has shown greater agreement with experimental data than the model of equivalent spheres used in [8]. However, the remaining discrepancies are not likely to be solved by yet another, better model. The LHP crystals used in this section are self-assembled polymorphs, and can thus contain significant inelastic strain which would then severely affect the results. There will also be a need for further experiments with higher resolution to examine the small crystals better, as we currently have no way to determine whether we are observing a single crystal or a cluster of smaller crystals, which would then result in the convolution of PL emission spectra and again negatively impact our results.

Conclusion

Throughout this thesis, I have laid out a possible approach to acquiring a correct band structure and value of band gap of a CsPbBr$_3$ bulk via the DFT method and my subsequent use of the theoretical data in a quantum mechanical model used to assess experimental data provided by Ing. Petr Liška a Ing. Michal Horák, PhD.

To obtain an authentic model of a CsPbBr$_3$ crystal we opted to start from an experiment. We used high-resolution images of CsPbBr$_3$ nanocrystals from TEM (by Ing. Michal Horák). Processing the data and using the normal distribution we procured the experimental value of the lattice parameter of CsPbBr$_3$ $a_e = (5.9 \pm 0.2)$ Å. We proceeded to carry out volume optimization calculations in VASP in a 7 % interval around a_e. The data we calculated was plotted out, showing the relation between the volume of the unit cell and the free energy of its atoms aiming to find the volume with the least free energy. To do so we fitted the data with the Murnaghan equation of state. The minimum of the fit showed the ideal theoretical lattice constant to be $a_t = 5.92$ Å. We were also able to obtain other data from the fit, the bulk modulus of our calculated CsPbBr$_3$ crystal, using the PBE functional, was calculated as $B = 20.28$ GPa, and the cohesive energy of the bulk $E_{coh} = -4.13$ eV.

With the ideal value of the lattice constant and therefore the ideal model of the structure we were able to progress to attempting to calculate the correct band structure and band gap of the CsPbBr$_3$ bulk. In the first stage of the way, we used classical DFT to calculate the band structure and DOS of the bulk, while implementing the effect of spin-orbital coupling. The first obtained band structure was seemingly consistent with the structure found in literature in regards to the shape of the bands, however, the value of the band gap was severely lacking. The value was calculated as $E_g = 0.77$ eV, this was the result of the combination of classical DFT's underestimation of the unoccupied states in the conduction band and the effect of the spin-orbital coupling. In the calculated DOS we observed a valence band containing mainly Pb orbitals and a conduction band consisting of a combination of Br and Pb orbitals, in agreement with what was suggested in [21].

In our continuous attempt to improve the value of the band gap we opted to implement the HSE hybrid functionals, which mix the classical DFT with a contribution from the Hartree-Fock (HF) method. At first we chose 25 % mixing of the HF energy contributions, which resulted the improvement to the value of the band gap to $E_g = 1.39$ eV. This was however insufficient and we chose to increase the HF contribution mixing to 45 %. This choice lead to further enhancement of the band gap. The resulting value was $E_g = 2.01$ eV. To ensure the physics of the calculated bands remain intact we also

calculated the value of effective mass for hole and electron at the R point, the point at which the transition occurs, at every step. To reach the experimentally acquired value of the band gap $E_\mathrm{g} = 2.36\,\mathrm{eV}$ we opted to implement the scissor operator, a mathematical operator which shifts the conduction band levels by a fixed constant.

To compare the data we calculated for a CsPbBr$_3$ bulk with the experimental data measured on nanocrystals we implemented a quantum mechanical model of an exciton in a finite potential well of arbitrary shape. This model utilizes a single-band effective-mass approximation of the Schrödinger equation to calculate the exciton energy levels. Based on the data at our disposal we considered two possible shapes of the potential well – a triangle shape and a lens shape. The triangle shapes showed no agreement with the theory, due to the small size of the nanocrystals and proximity of said nanocrystals to each other, which resulted in skewed PL emission peak wavelength values and those then negatively affected the experimental energy compared with the theoretical model.

The lens shapes have shown greater agreement with the experiment both in the trend of the relation between the size of the nanocrystal and the PL emission energy and also in the actual values of the emission energy for each crystal. The best agreement was achieved in larger nanocrystals as they exhibit a more favourable noise-to-signal ratio than the smaller ones. The remaining discrepancies are due to the nanocrystals' being self-assembled polymorphs, which can contain significant inelastic strain which severely impacts the results.

Bibliography

1. CELÝ, J. *Kvazičástice v pevných látkách*. 2. vyd. Praha: VUTIUM, 2004. ISBN 978-80-214-2611-5.

2. GRIFFITHS, D. J.; SCHROETER, D. F. *Introduction to Quantum Mechanics*. Cambridge University Press, 2018-09-12. ISBN 9781316995433. Available from DOI: `10.1017/9781316995433`.

3. PARR, R. G.; WEITAO, Y. *Density-Functional Theory of Atoms and Molecules*. Oxford University Press, 1995-01-05. ISBN 9780195092769. Available from DOI: `10.1093/oso/9780195092769.001.0001`.

4. KITTEL, C. *Introduction to solid state physics*. 8th ed. Hoboken: John Wiley & Sons, c2005. ISBN 978-0-471-41526-8.

5. ALDARAGHMEH, T. *STUDY OF SOME ELECTRICAL PROPERTIES OF UNDOPED LEAD IODIDE THIN FILMS DEPOSITED BY FLASH-EVAPORATION METHOD AT SUBSTRATE TEMPERATURES BETWEEN 150 o C AND 200 o C*. 2013-05. Available from DOI: `10.13140/RG.2.2.32039.65440`. PhD thesis.

6. YU, P. Y.; CARDONA, M. *Fundamentals of Semiconductors*. Berlin, Heidelberg: Springer Berlin Heidelberg, 2010. ISBN 978-3-642-00709-5. Available from DOI: `10.1007/978-3-642-00710-1`.

7. HOLGATE, S. A. *Understanding Solid State Physics*. Second edition. | Boca Raton: CRC Press: CRC Press, 2021-4-2. ISBN 9780429288234. Available from DOI: `10.1201/9780429288234`.

8. LIŠKA, P. *Optická charakterizace pokročilých nanomateriálů s vysokým laterálním rozlišením*. Brno, 2021. Diplomová práce. Vysoké učení technické v Brně. Fakulta strojního inženýrství. Ústav fyzikálního inženýrství.

9. FRENKEL, J. On the Transformation of light into Heat in Solids. I. *Physical Review*. 1931, **37**(1), 17–44. ISSN 0031-899X. Available from DOI: `10.1103/PhysRev.37.17`.

10. WANNIER, G. H. The Structure of Electronic Excitation Levels in Insulating Crystals. *Physical Review*. 1937, **52**(3), 191–197. ISSN 0031-899X. Available from DOI: `10.1103/PhysRev.52.191`.

11. FOX, M. *Optical properties of solids*. 2nd ed. Oxford: Oxford University Press, 2010. ISBN 9780199573363.

12. VIJ, D. R. *Luminescence of Solids*. 1st edition. Plenum Press, New York: Springer, Boston, MA, 1998. ISBN 978-1-4615-5361-8. Available from DOI: `10.1007/978-1-4615-5361-8`.

13. MOMMA, K.; IZUMI, F. VESTA3 for three-dimensional visualization of crystal, volumetric and morphology data. *Journal of Applied Crystallography*. 2011, **44**(6), 1272–1276. ISSN 0021-8898. Available from DOI: `10.1107/S0021889811038970`.

14. KOVALENKO, M. V.; PROTESESCU, L.; BODNARCHUK, M. I. Properties and potential optoelectronic applications of lead halide perovskite nanocrystals. *Science*. 2017-11-10, **358**(6364), 745–750. ISSN 0036-8075. Available from DOI: `10.1126/science.aam7093`.

15. AKKERMAN, Q. A.; RAINÒ, G.; KOVALENKO, M. V. et al. Genesis, challenges and opportunities for colloidal lead halide perovskite nanocrystals. *Nature Materials*. 2018, **17**(5), 394–405. ISSN 1476-1122. Available from DOI: `10.1038/s41563-018-0018-4`.

16. HAEGER, T.; HEIDERHOFF, R.; RIEDL, T. Thermal properties of metal-halide perovskites. *Journal of Materials Chemistry C*. 2020-10-29, **8**(41), 14289–14311. ISSN 2050-7526. Available from DOI: `10.1039/D0TC03754K`.

17. TILLEY, R. J. D. *Perovskites*. Chichester, UK: John Wiley & Sons, Ltd, 2016-05-06. ISBN 9781118935651. Available from DOI: `10.1002/9781118935651`.

18. YANG, D.; CAO, M.; ZHONG, Q. et al. All-inorganic cesium lead halide perovskite nanocrystals: synthesis, surface engineering and applications. *Journal of Materials Chemistry C*. 2019-01-24, **7**(4), 757–789. ISSN 2050-7526. Available from DOI: `10.1039/C8TC04381G`.

19. AGORA, J. O.; OTIENO, C.; NYAWERE, P. W. et al. Ab initio study of pressure induced phase transition, structural and electronic structure properties of superconducting perovskite compound GdBa2Cu3O7-x. *Computational Condensed Matter*. 2020, **23**. ISSN 23522143. Available from DOI: `10.1016/j.cocom.2020.e00461`.

20. HUSSAIN, M.; RASHID, M.; SAEED, F. et al. Spin–orbit coupling effect on energy level splitting and band structure inversion in CsPbBr3. *Journal of Materials Science*. 2021, **56**(1), 528–542. ISSN 0022-2461. Available from DOI: `10.1007/s10853-020-05298-8`.

21. BECKER, M. A.; VAXENBURG, R.; NEDELCU, G. et al. Bright triplet excitons in caesium lead halide perovskites. *Nature*. 2018, **553**(7687), 189–193. ISSN 0028-0836. Available from DOI: `10.1038/nature25147`.

22. BIHLMAYER, G.; RADER, O.; WINKLER, R. Focus on the Rashba effect. *New Journal of Physics*. 2015, **17**(5). ISSN 1367-2630. Available from DOI: `10.1088/1367-2630/17/5/050202`.

23. PARK, S. R.; KIM, C. Microscopic mechanism for the Rashba spin-band splitting: Perspective from formation of local orbital angular momentum. *Journal of Electron Spectroscopy and Related Phenomena*. 2015, **201**, 6–17. ISSN 03682048. Available from DOI: `10.1016/j.elspec.2014.12.009`.

24. RAINÒ, G.; NEDELCU, G.; PROTESESCU, L. et al. Single Cesium Lead Halide Perovskite Nanocrystals at Low Temperature: Fast Single-Photon Emission, Reduced Blinking, and Exciton Fine Structure. *ACS Nano*. 2016-02-23, **10**(2), 2485–2490. ISSN 1936-0851. Available from DOI: `10.1021/acsnano.5b07328`.

25. KANE, E. Chapter 3 The k •p Method. In: Elsevier, 1966, pp. 75–100. ISBN 9780127521015. Available from DOI: `10.1016/S0080-8784(08)62376-5`.

26. LANDAU, L. D.; LIFŠIC, J. M. *Course of theoretical physics*. 3rd ed., rev. and enl. Amsterdam: Butterworth-Heinemann, 2003. ISBN 9780750635394.

27. ZHOU, Y.; CHEN, J.; BAKR, O. M. et al. Metal-Doped Lead Halide Perovskites: Synthesis, Properties, and Optoelectronic Applications. *Chemistry of Materials*. 2018-10-09, **30**(19), 6589–6613. ISSN 0897-4756. Available from DOI: `10.1021/acs.chemmater.8b02989`.

28. SHEN, W.; CHEN, J.; WU, J. et al. Nonlinear Optics in Lead Halide Perovskites: Mechanisms and Applications. *ACS Photonics*. 2021-01-20, **8**(1), 113–124. ISSN 2330-4022. Available from DOI: `10.1021/acsphotonics.0c01501`.

29. FU, Y.; ZHU, H.; SCHRADER, A. W. et al. Nanowire Lasers of Formamidinium Lead Halide Perovskites and Their Stabilized Alloys with Improved Stability. *Nano Letters*. 2016-02-10, **16**(2), 1000–1008. ISSN 1530-6984. Available from DOI: `10.1021/acs.nanolett.5b04053`.

30. FU, Y.; ZHU, H.; STOUMPOS, C. C. et al. Broad Wavelength Tunable Robust Lasing from Single-Crystal Nanowires of Cesium Lead Halide Perovskites (CsPbX 3 , X = Cl, Br, I). *ACS Nano*. 2016-08-23, **10**(8), 7963–7972. ISSN 1936-0851. Available from DOI: `10.1021/acsnano.6b03916`.

31. GUHRENZ, C.; BENAD, A.; ZIEGLER, C. et al. Solid-State Anion Exchange Reactions for Color Tuning of CsPbX 3 Perovskite Nanocrystals. *Chemistry of Materials*. 2016-12-27, **28**(24), 9033–9040. ISSN 0897-4756. Available from DOI: `10.1021/acs.chemmater.6b03980`.

32. QUAN, L. N.; QUINTERO-BERMUDEZ, R.; VOZNYY, O. et al. Highly Emissive Green Perovskite Nanocrystals in a Solid State Crystalline Matrix. *Advanced Materials*. 2017, **29**(21). ISSN 09359648. Available from DOI: `10.1002/adma.201605945`.

33. SAKURAI, J. J.; NAPOLITANO, J. *Modern Quantum Mechanics*. Cambridge University Press, 2018-06-21. ISBN 9781108499996. Available from DOI: `10.1017/9781108499996`.

34. TYC, T. *Teoretická mechanika - poznámky k přednáškám*. 2021.

35. HOHENBERG, P.; KOHN, W. Inhomogeneous Electron Gas. *Physical Review*. 1964, **136**(3B), B864–B871. ISSN 0031-899X. Available from DOI: `10.1103/PhysRev.136.B864`.

36. BAGAYOKO, D. Understanding density functional theory (DFT) and completing it in practice. *AIP Advances*. 2014, **4**(12). ISSN 2158-3226. Available from DOI: `10.1063/1.4903408`.

37. VOSKO, S. H.; WILK, L.; NUSAIR, M. Accurate spin-dependent electron liquid correlation energies for local spin density calculations: a critical analysis. *Canadian Journal of Physics*. 1980-08-01, **58**(8), 1200–1211. ISSN 0008-4204. Available from DOI: `10.1139/p80-159`.

38. DIRAC, P. A. M. Note on Exchange Phenomena in the Thomas Atom. *Mathematical Proceedings of the Cambridge Philosophical Society*. 1930, **26**(3), 376–385. ISSN 0305-0041. Available from DOI: `10.1017/S0305004100016108`.

39. CHACHIYO, T. Communication: Simple and accurate uniform electron gas correlation energy for the full range of densities. *The Journal of Chemical Physics*. 2016-07-14, **145**(2). ISSN 0021-9606. Available from DOI: `10.1063/1.4958669`.

40. OLIVER, G. L.; PERDEW, J. P. Spin-density gradient expansion for the kinetic energy. *Physical Review A*. 1979, **20**(2), 397–403. ISSN 0556-2791. Available from DOI: `10.1103/PhysRevA.20.397`.

41. PERDEW, J. P.; CHEVARY, J. A.; VOSKO, S. H. et al. Atoms, molecules, solids, and surfaces: Applications of the generalized gradient approximation for exchange and correlation. *Physical Review B*. 1992, **46**(11), 6671–6687. ISSN 0163-1829. Available from DOI: `10.1103/PhysRevB.46.6671`.

42. PERDEW, J. P.; BURKE, K.; ERNZERHOF, M. Generalized Gradient Approximation Made Simple. *Physical Review Letters*. 1996, **77**(18), 3865–3868. ISSN 0031-9007. Available from DOI: `10.1103/PhysRevLett.77.3865`.

43. HELLMANN, H. A New Approximation Method in the Problem of Many Electrons. *The Journal of Chemical Physics*. 1935, **3**(1), 61–61. ISSN 0021-9606. Available from DOI: `10.1063/1.1749559`.

44. TOPP, W. C.; HOPFIELD, J. J. Chemically Motivated Pseudopotential for Sodium. *Physical Review B*. 1973, **7**(4), 1295–1303. ISSN 0556-2805. Available from DOI: `10.1103/PhysRevB.7.1295`.

45. SCHWERDTFEGER, P. The Pseudopotential Approximation in Electronic Structure Theory. *ChemPhysChem*. 2011-12-09, **12**(17), 3143–3155. ISSN 14394235. Available from DOI: `10.1002/cphc.201100387`.

46. WIDAYANI, W.; WUNGU, T. D. K.; MARSHA, S. E. et al. Study of Target Recognition of MAA-based Molecularly Imprinted Polymer (MIP) Using Density Functional Theory (DFT) Computation on the Interaction of Methacrylic Acid (MAA)-D-Glucose. *Journal of Polymer and Biopolymer Physics Chemistry*. 2017, **5**(1), 10–12. ISSN 2373-3411. Available from DOI: `10.12691/jpbpc-5-1-2`.

47. KRESSE, G.; HAFNER, J. Ab initio molecular dynamics for liquid metals. *Phys. Rev. B.* 1993-01, **47**, 558–561. Available from DOI: `10.1103/PhysRevB.47.558`.

48. KRESSE, G.; HAFNER, J. Ab initio molecular-dynamics simulation of the liquid-metal–amorphous-semiconductor transition in germanium. *Phys. Rev. B.* 1994-05, **49**, 14251–14269. Available from DOI: `10.1103/PhysRevB.49.14251`.

49. KRESSE, G.; FURTHMÜLLER, J. Efficiency of ab-initio total energy calculations for metals and semiconductors using a plane-wave basis set. *Computational Materials Science.* 1996, **6**(1), 15–50. ISSN 0927-0256. Available from DOI: `https://doi.org/10.1016/0927-0256(96)00008-0`.

50. KRESSE, G.; FURTHMÜLLER, J. Efficient iterative schemes for ab initio total-energy calculations using a plane-wave basis set. *Phys. Rev. B.* 1996-10, **54**, 11169–11186. Available from DOI: `10.1103/PhysRevB.54.11169`.

51. *The VASP Manual* [online]. MediaWiki: VASPWiki, 2022-04-11 [visited on 2022-04-30]. Available from: `<https://www.vasp.at/wiki/index.php/The_VASP_Manual>`.

52. NEČAS, D.; KLAPETEK, P. Gwyddion: an open-source software for SPM data analysis. *Central European Journal of Physics.* 2012, **10**, 181–188. ISSN 1895-1082. Available from DOI: `10.2478/s11534-011-0096-2`.

53. WANG, Y. *VASP: Computing Bulk Modulus of Au.* Stanford, CA, 2015.

54. VERMA, A.; KUMAR, A. Bulk modulus of cubic perovskites. *Journal of Alloys and Compounds.* 2012, **541**, 210–214. ISSN 09258388. Available from DOI: `10.1016/j.jallcom.2012.07.027`.

55. GUNER, T.; AKBALI, B.; OZCAN, M. et al. Monitoring the Doping and Diffusion Characteristics of Mn Dopants in Cesium Lead Halide Perovskites. *The Journal of Physical Chemistry C.* 2018-05-31, **122**(21), 11543–11549. ISSN 1932-7447. Available from DOI: `10.1021/acs.jpcc.8b02580`.

56. PERDEW, J. P.; BURKE, K.; ERNZERHOF, M. Generalized Gradient Approximation Made Simple. *Phys. Rev. Lett.* 1996-10, **77**, 3865–3868. Available from DOI: `10.1103/PhysRevLett.77.3865`.

57. PERDEW, J. P.; BURKE, K.; ERNZERHOF, M. Perdew, Burke, and Ernzerhof Reply: *Phys. Rev. Lett.* 1998-01, **80**, 891–891. Available from DOI: `10.1103/PhysRevLett.80.891`.

58. SCOTT, R. A. *Encyclopedia of Inorganic and Bioinorganic Chemistry.* Chichester, UK: John Wiley & Sons, Ltd, 2011-12-15. ISBN 9781119951438.

59. ERNZERHOF, M.; SCUSERIA, G. E. Assessment of the Perdew–Burke–Ernzerhof exchange-correlation functional. *The Journal of Chemical Physics.* 1999-03-15, **110**(11), 5029–5036. ISSN 0021-9606. Available from DOI: `10.1063/1.478401`.

60. BORLIDO, P.; SCHMIDT, J.; HURAN, A. W. et al. Exchange-correlation functionals for band gaps of solids: benchmark, reparametrization and machine learning. *Npj Computational Materials.* 2020, **6**(1). ISSN 2057-3960. Available from DOI: `10.1038/s41524-020-00360-0`.

61. BLÖCHL, P. E. Projector augmented-wave method. *Phys. Rev. B.* 1994-12, **50**, 17953–17979. Available from DOI: `10.1103/PhysRevB.50.17953`.

62. KRESSE, G.; JOUBERT, D. From ultrasoft pseudopotentials to the projector augmented-wave method. *Phys. Rev. B.* 1999-01, **59**, 1758–1775. Available from DOI: `10.1103/PhysRevB.59.1758`.

63. WANG, V.; XU, N.; LIU, J.-C. et al. VASPKIT: A user-friendly interface facilitating high-throughput computing and analysis using VASP code. *Computer Physics Communications.* 2021, **267**, 108033. Available from DOI: `https://doi.org/10.1016/j.cpc.2021.108033`.

64. LEVINE, Z. H.; ALLAN, D. C. Linear optical response in silicon and germanium including self-energy effects. *Physical Review Letters.* 1989, **63**(16), 1719–1722. ISSN 0031-9007. Available from DOI: `10.1103/PhysRevLett.63.1719`.

65. GONZE, X.; LEE, C. Dynamical matrices, Born effective charges, dielectric permittivity tensors, and interatomic force constants from density-functional perturbation theory. *Physical Review B.* 1997, **55**(16), 10355–10368. ISSN 0163-1829. Available from DOI: `10.1103/PhysRevB.55.10355`.

66. WANG, C.-Y.; ELLIOTT, P.; SHARMA, S. et al. Real time scissor correction in TD-DFT. *Journal of Physics: Condensed Matter.* 2019-05-29, **31**(21). ISSN 0953-8984. Available from DOI: `10.1088/1361-648X/ab048a`.

67. HEDIN, L. New Method for Calculating the One-Particle Green's Function with Application to the Electron-Gas Problem. *Physical Review.* 1965, **139**(3A), A796–A823. ISSN 0031-899X. Available from DOI: `10.1103/PhysRev.139.A796`.

68. ARYASETIAWAN, F.; GUNNARSSON, O. The GW method. *Reports on Progress in Physics.* 1998-03-01, **61**(3), 237–312. ISSN 0034-4885. Available from DOI: `10.1088/0034-4885/61/3/002`.

69. NGO, C. Y.; YOON, S. F.; FAN, W. J. et al. Effects of size and shape on electronic states of quantum dots. *Phys. Rev. B.* 2006-12, **74**, 245331. Available from DOI: `10.1103/PhysRevB.74.245331`.

70. TOGO, A.; TANAKA, I. First principles phonon calculations in materials science. *Scr. Mater.* 2015-11, **108**, 1–5.

List of abbreviations

NSC . . . .   Non-Self-Consistent
SC . . . .   Self-Consistent
GGA . . . .   Generalized Gradient Approximation
LSDA . . . .   Local Spin Density Approximation
LDA . . . .   Local-Density Approximation
PL . . . .   Photoluminescence
DOS . . . .   Density of States
LHP . . . .   Lead Halide Perovskites
DFT . . . .   Density Functional Theory
SE . . . .   Schrödinger Equation

A. The VASP Files

Here you can find the files used in our calculations in full.

A.1 VASP Input Files

The POSCAR file specifies the structure.

```
CsPbBr3
   5.92
     1.0200333401049706     0.0000000000000000     0.0000000000000000
     0.0000000000000000     1.0200333401049706     0.0000000000000000
     0.0000000000000000     0.0000000000000000     1.0200333401049706
   Cs    Pb    Br
     1     1     3
Direct
  0.0000000000000000   0.0000000000000000   0.0000000000000000
  0.5000000000000000   0.5000000000000000   0.5000000000000000
  0.5000000000000000   0.5000000000000000   0.0000000000000000
  0.0000000000000000   0.5000000000000000   0.5000000000000000
  0.5000000000000000   0.0000000000000000   0.5000000000000000

  0.00000000E+00   0.00000000E+00   0.00000000E+00
  0.00000000E+00   0.00000000E+00   0.00000000E+00
  0.00000000E+00   0.00000000E+00   0.00000000E+00
  0.00000000E+00   0.00000000E+00   0.00000000E+00
  0.00000000E+00   0.00000000E+00   0.00000000E+00
```

The first line is viewed by the program as a comment line and usually contains the name of the system. The second line is where we find the universal scaling factor, in our case the lattice constant of the crystal, which scales the lattice vectors. Those are on the lines three through five. The next two lines specify the type of atoms and the number of each atomic species. The eighth line signifies whether the atomic coordinates are input in Cartesian or Direct coordinates. On lines following come the atomic coordinates.

The KPOINTS file determines the sampling of the reciprocal space.

```
K-Points
 0
Monkhorst Pack
 6  6  6
  0  0  0
```

The zero on the second line means automatic generation. The third line specifies the k-points have been generated using the Monkhorst-Pack scheme, Gamma centred or Cartesian can be also used. Numbers on the fourth line serve to determine the number of subdivisions along the reciprocal lattice. The fifth line gives an additional shift of the k-mesh. This type of sampling is used in structure relaxation or DOS calculations.

```
Special k-points for band structure
100 ! 100 intersections
line-mode
Reciprocal
     0.0000000000    0.0000000000    0.0000000000 1    GAMMA
     0.0000000000    0.5000000000    0.0000000000 1    X


     0.0000000000    0.5000000000    0.0000000000 1    X
     0.5000000000    0.5000000000    0.0000000000 1    M


     0.5000000000    0.5000000000    0.0000000000 1    M
     0.0000000000    0.0000000000    0.0000000000 1    GAMMA


     0.0000000000    0.0000000000    0.0000000000 1    GAMMA
     0.5000000000    0.5000000000    0.5000000000 1    R


     0.5000000000    0.5000000000    0.5000000000 1    R
     0.0000000000    0.5000000000    0.0000000000 1    X


     0.5000000000    0.5000000000    0.5000000000 1    R
     0.5000000000    0.5000000000    0.0000000000 1    M
```

The second line specifies the number of points per line segment. The `line-mode` on the third line ensures the generation of a string of k-points between every two specified points in the first Brillouin zone. The fourth line determines the format in which the coordinates of the points will be provided. The rest are coordinates of points of high symmetry in the first Brillouin zone. This type of `KPOINTS` file is to be used in band structure calculations.

The `INCAR` file is where we specify the calculation's parameters.

```
System = CsPbBr3
###
ISTART = 0
ICHARG = 2


smearing:
 ISMEAR = 0


electronic:
 LREAL  = .False.
 ALGO   = A
 ENCUT  = 400
 NELM = 100
 LMAXMIX = 4
 EDIFF = 1E-6
 NBANDS = 64


fft:
 PREC   = Accurate


ionic:
 IBRION = 2
 ISIF   = 4
 NSW    = 30
 EDIFFG = -0.005


dft:
 LSORBIT = .TRUE.


parallel:
 NCORE  = 8
 KPAR   = 2
```

The capitalized words are called *tags*. `ISTART` tells the program where to start, 0 means a new job, and with 1 the program would start from previously calculated wave functions from the `WAVECAR`. `ICHARG` determines how VASP constructs the initial charge density, 2 means the program uses the sum of the atomic charge densities. `ENCUT` gives the cut-off energy for the set of the plane-wave-basis. `ISMEAR` specifies the method used for the electron smearing, 1 means the Fermi smearing. `SIGMA` defines the interval over which the smearing happens. `IBRION` establishes how the ions are treated depending on the type of calculation, 2 is for the ionic relaxation using the conjugated gradient method. `NSW` sets the maximum number of ionic steps. `EDIFF` gives the condition both the total energy change and the band-structure energy change must clear in order for the calculation to stop. `ISYM` switches on or off the consideration of symmetry. `KPAR`

and `NCORE` along with others serve to optimize the given calculation.

A.2 VASP Output Files

The `OUTCAR` file contains the complete output provided by VASP.

A.3 Stages of the Calculation

The following excerpts from `INCAR` files include only tags that are unique to the given process, every `INCAR` file should also include all the appropriate tags such as those shown in the `INCAR` file in the Input section above.

Volume Relaxation

```
ISMEAR = -5
ISIF   = 4
NSW    = 30
```

Spin-Orbital Coupling

First step:

```
 PREC = Accurate
 ISYM = -1
 LREAL = .FALSE.
 LSORBIT = .TRUE.
```

This calculation already takes into account the effect of the spin-orbital coupling (`LSORBIT = .TRUE.`).

The second step is mostly identical to the first one but for the addition of `ICHARG = 11` to the `INCAR` file.

25% Hartree-Fock Mixing

```
LHFCALC = .TRUE.
HFSCREEN = 0.2
AEXX = 0.25
ALGO = D
TIME = 0.4
LDIAG = .TRUE.
```

45% Hartree-Fock Mixing

This calculation is virtually identical to the one before with the only difference being

```
AEXX = 0.45
```

B. The Phonon calculations

For the phonon calculation, we opted for the finite displacement method. In this method certain atoms in a lattice are displaced by a small amount from their equilibrium, then single-point energy calculations are conducted and the forces on every ion in the system are evaluated. For conducting the phonon calculations we used an open-source code `phonopy` [70], while VASP was used for the heavy-duty work of classical DFT calculations.

The phonon calculations ought to start with well-relaxed structure and we have such structure already prepared and ready to go. The first step takes place in `phonopy`, where we calculate a $3 \times 3 \times 3$ supercell from our pre-existing `POSCAR` file. We do so by running the following command:

```
phonopy -d --dim="3 3 3"
```

We obtain a set of three `POSCAR` files each containing the supercell with the single atom displacements.

The goal of the second step is to obtain force constants for the supercell. We need to carry out a set of three static SC calculations in VASP, one for each of the `POSCAR` files, the result of which are calculated forces on an atom. It is important in this calculation for the evaluation of the projection operators to be done in reciprocal space because in reciprocal space the number of operators scales with the number of plane waves. Using the calculated forces on atom `phonopy` can construct a set of forces for the entire supercell written in a `FORCE_SETS` file. The `INCAR` used for the mentioned SC calculations of force constants should contain these tags

```
LREAL   = .FALSE.
ISYM    = 0
ADDGRID = .TRUE.
```

It is advised to use fewer k-points to conserve the size of the overall structure over which the calculations are carried out. We used a $6 \times 6 \times 6$ k-point grid in our regular DFT calculations, therefore now when considering a supercell $3 \times 3 \times 3$, we should lower the k-points to $2 \times 2 \times 2$.

Once the DFT calculations are complete for all three of the `POSCAR` files, we return to `phonopy`, where we create the force set from the force constants contained `vasprun.xml` files, which we place in three folders `disp-001--003`. The command for the creation of force set is as follows:

```
phonopy -f disp-{001..003}/vasprun.xml
```

The output is a `FORCE_SET` file. Now we move on to the post-process. During the post-process, the force constants are calculated from the set of forces, from those a part of the dynamical matrix is built and finally from the dynamical matrices the eigenvectors and phonon frequencies are calculated in the specified q-points.

For the mesh sampling calculations, we need a file that will define the process. In it, we specify the type of atoms in the structure, the dimensions and the mesh sampling in a scheme of our choice, which was Monkhorst-Pack. The file is `mesh.conf`:

```
ATOM_NAME = Cs Pb Br
DIM = 3 3 3
MP = 48 48 48
```

The DOS is then calculated, plotted and saved with:

```
phonopy -p -s mesh.conf
```

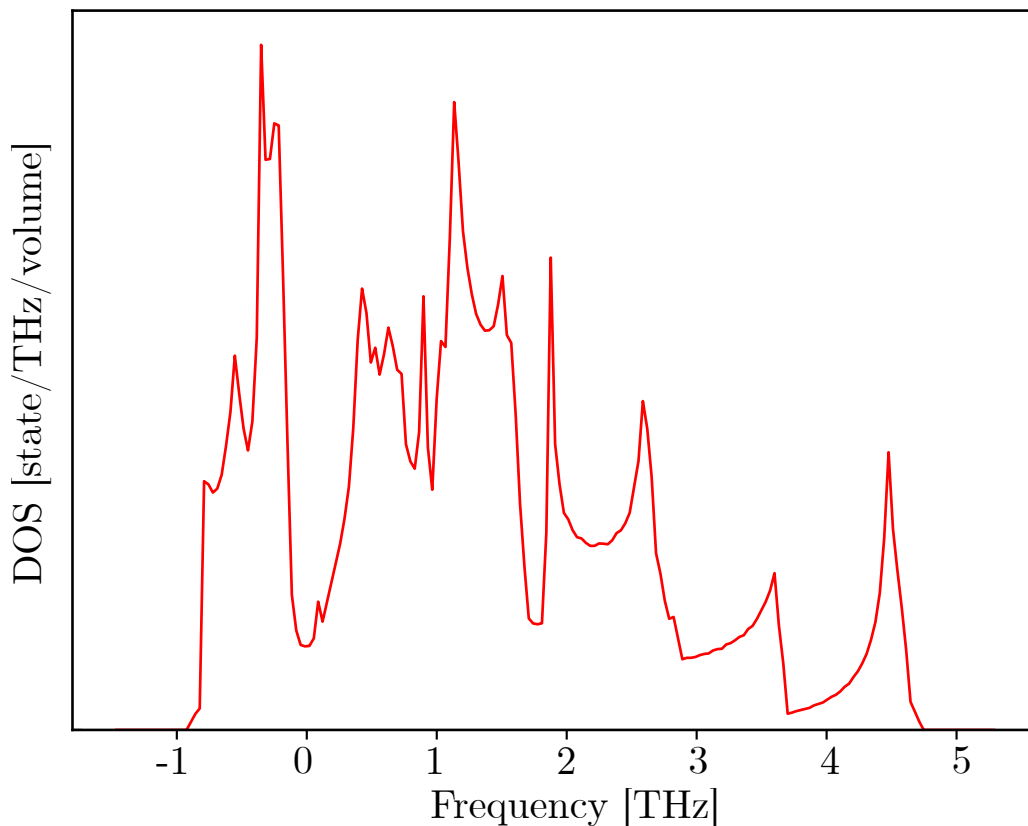The resulting phonon DOS is in Figure B.1.

Figure B.1: The phonon total DOS.

For the band structure calculations we need to write a file specifying the band structure calculation, it is `band.conf`:

```
ATOM_NAME = Cs Pb Br
DIM = 3 3 3
BAND = 0.0 0.0 0.0  0.0 0.5 0.0  0.0 0.5 0.0   0.5 0.5 0.0  0.5 0.5
0.0  0.0 0.0 0.0   0.0 0.0 0.0  0.5 0.5 0.5  0.5 0.5 0.5   0.0 0.5 0.0  0.5
0.5 0.5  0.5 0.5 0.0
```
which has to specify the types of atoms used, the dimensions of the supercell and the sampling of the first Brillouin zone. The band structure plotting is initiated by the following command:

```
phonopy -p -s band.conf
```

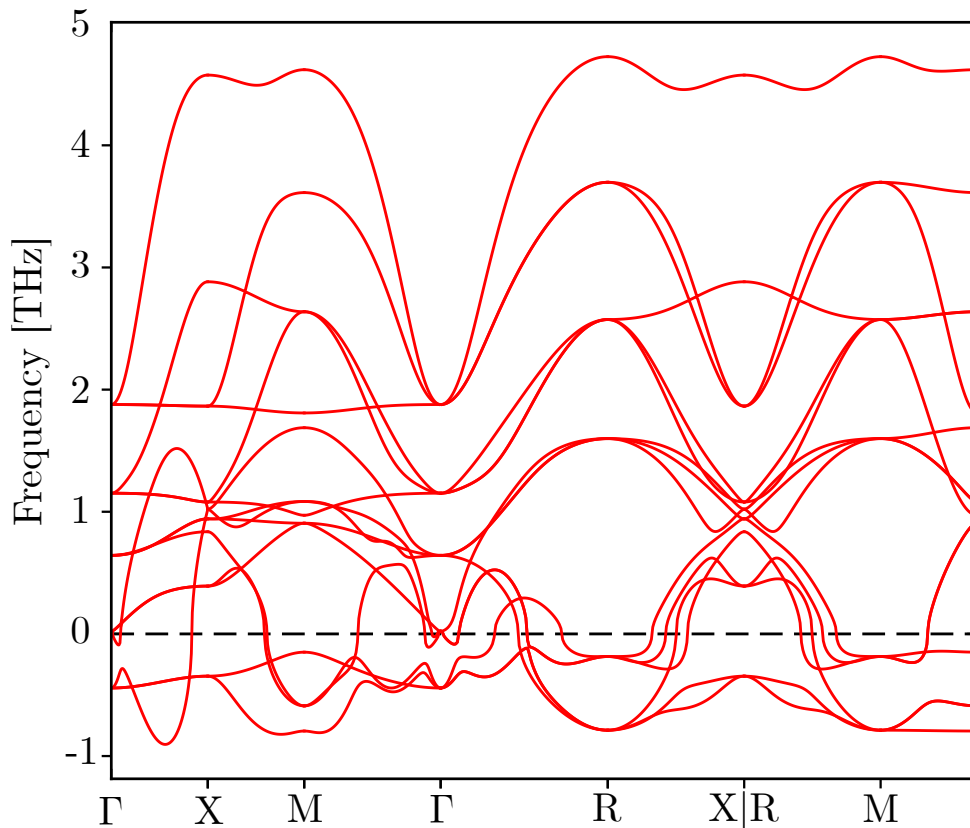The result of our calculation is shown in Figure B.2.

Figure B.2: The phonon band structure.

In both Figure B.1 and B.2 we see the calculated frequencies go into negative values. That is the problem we were not able to solve in the course of the writing of this thesis. However, after consulting this problem with people with experienced we have found out that the problem was most likely in the use of the simple cubic lattice, which we employed for simplicity of the calculations. Simple cubic crystal of $CsPbBr_3$, however, is not stable at 0 K. The calculations would therefore need to be run using the orthorhombic phase of $CsPbBr_3$, which was not possible with our current resources.